Strength, Depth, and Geometry of Magnetic Sources in the Crust of the Moon From Localized Power Spectrum Analysis

Mark Wieczorek

AGU PUBLICATIONS

JGR

Journal of Geophysical Research: Planets

RESEARCH ARTICLE
10.1002/2017JE005418

Key Points:
- Lunar crustal magnetism is investigated using a localized power spectrum analysis
- Most magnetization is deep in the crust and dates from the first 100 Myr of lunar history
- A nearside province has extremely low field strengths as a result of high crustal temperatures

Correspondence to:
M. A. Wieczorek,
mark.wieczorek@oca.eu

Citation:
Wieczorek, M. A. (2018). Strength, depth, and geometry of magnetic sources in the crust of the Moon from localized power spectrum analysis. *Journal of Geophysical Research: Planets, 123,* 291–316. https://doi.org/10.1002/2017JE005418

Received 10 AUG 2017
Accepted 21 DEC 2017
Accepted article online 5 JAN 2018
Published online 30 JAN 2018

Strength, Depth, and Geometry of Magnetic Sources in the Crust of the Moon From Localized Power Spectrum Analysis

Mark A. Wieczorek[1]

[1] Université Côte d'Azur, Observatoire de la Côte d'Azur, CNRS, Laboratoire Lagrange, Nice, France

Abstract Spacecraft observations show that weak magnetic fields of crustal origin are ubiquitous across the surface of the Moon. To investigate the origin of these magnetic anomalies, a model was developed for the magnetic power spectrum that consists of ensembles of randomly magnetized sills or prisms. Localized spectrum analyses constrained how the parameters of this model vary with position, including the size of the sources, a quantity proportional to their mean-squared dipole moment, and the depth to the top and bottom of the magnetized region. The depth to the top of the magnetized region varies from the surface to about 25 km. The magnetic carriers in the deep crust likely formed at the same time as the crust itself, implying that a core-generated dynamo field must have existed when the crust was cooling during the first 100 Myr of lunar evolution. The parameter related to the strength of magnetization shows the existence of a prominent region on the nearside hemisphere that is largely unmagnetized and that correlates with a region of extremely low surface field strengths. This region lies entirely within a geological province that is highly enriched in heat-producing elements (the Procellarum KREEP Terrane), suggesting that this region escaped being magnetized because of prolonged high crustal temperatures. The nearside magnetic low may be representative of the size of that portion of the crust that is highly enriched in heat-producing elements, which is almost one third the size of the Procellarum KREEP Terrane based on surface thorium abundances.

1. Introduction

The Moon today does not have a global magnetic field generated by a core dynamo, yet orbital magnetic field data show the existence of strong crustal magnetic anomalies and paleomagnetic analyses show that some lunar rocks are strongly magnetized (for reviews, see Fuller & Cisowski, 1987; Weiss & Tikoo, 2014). The simplest explanation for these observations is that the core of the Moon once generated a magnetic field in its past that magnetized portions of the crust, and that as the Moon continued to cool over time, the dynamo eventually stopped when the heat escaping the core passed below some critical threshold value. A similar scenario has been proposed for the planet Mars (e.g., Acuña et al., 1999) that, like the Moon, has strong crustal magnetization but does not possess a present day core-generated magnetic field.

Even though this broad outline of lunar magnetism is widely accepted, lunar magnetism remains poorly understood with fundamental questions remaining about the timing and strength of the dynamo field, the nature of the sources that powered the dynamo, and the origin of the magnetic carriers that are responsible for crustal magnetization (e.g., Weiss & Tikoo, 2014). Paleomagnetic analyses of lunar samples have shown that a core dynamo likely operated between as early as about 4.25 Ga (Garrick-Bethell et al., 2009, 2017) and as late as somewhere between 1 and 2.5 Ga (Tikoo et al., 2017). The strength of the field on the surface is predicted to be similar to that of Earth up until 3.56 Ga Suavet et al. (2013), and afterward the surface field strength decreased by an order of magnitude (Tikoo et al., 2014, 2017). Several sources of power have been proposed to drive a lunar dynamo, including thermal convection (e.g., Evans et al., 2014; Konrad & Spohn, 1997), core crystallization with compositional convection (e.g., Laneuville et al., 2014; Scheinberg et al., 2015), precession of the solid mantle Dwyer et al. (2011), and short-lived perturbations in the Moon's rotation rate following large impact events Le Bars et al. (2011). Together, these sources could power continuously a long-lived dynamo lasting more than a billion years after Moon formation. Regardless, a longstanding unresolved issue is that the surface field strengths predicted by the dynamo models are more than 10 times smaller than required by the paleomagnetic measurements.

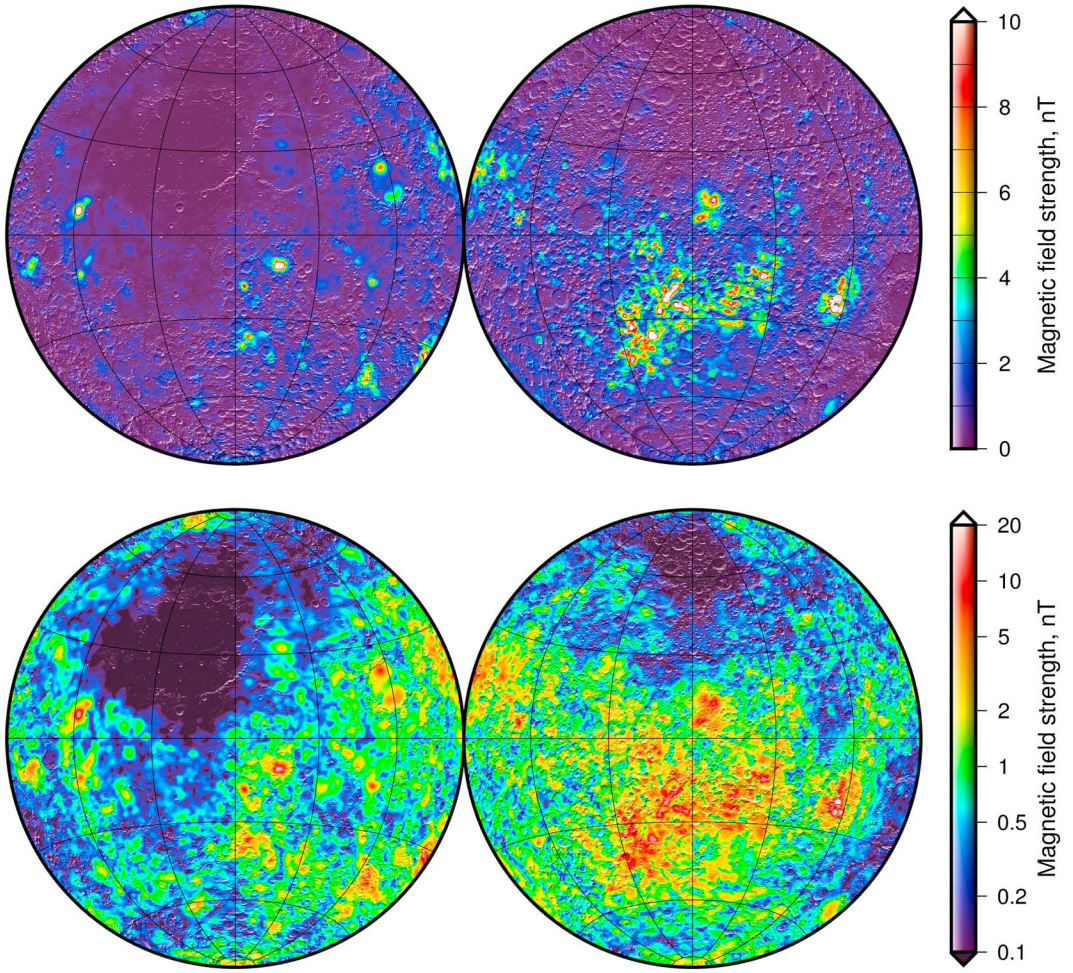

Figure 1. Total magnetic field strength of the Moon at 30 km altitude plotted using a (top) linear and (bottom) logarithmic color scale. The magnetic field was evaluated using a 449° and order spherical harmonic expansion of the model of Tsunakawa et al. (2015). The field strength maps are presented in Lambert azimuthal equal-area projections centered over the (left) nearside and (right) farside hemispheres and are overlain by a shaded relief map derived from the Lunar Orbiter Laser Altimeter Smith et al. (2010). Grid lines are spaced every 30° in latitude and longitude.

Another fundamental question concerning lunar magnetism is the origin of the magnetic carriers. Though it is well known that metallic iron alloyed with small quantities of nickel (kamacite) is the primary magnetic mineral in lunar rocks (e.g., Fuller & Cisowski, 1987), this metal could be either of lunar or meteoritic origin. Given that most endogenous crustal rocks have low concentrations of metallic iron, they are incapable of accounting for the strongest crustal magnetic anomalies observed from orbit Wieczorek et al. (2012). Recent studies have thus highlighted the importance of the delivery of metallic iron to the Moon from the projectiles that formed the largest impact basins. In one such study by Wieczorek et al. (2012), hydrocode simulations of the impact process have shown that if the giant farside South Pole-Aitken basin formed under oblique impact conditions, with the projectile traveling from south to north, projectile materials could have been deposited precisely where the largest grouping of farside magnetic anomalies is found. In another study by Oliveira et al. (2017), the impact melt sheets of several Nectarian-aged impact basins (including Mendel-Rydberg, Nectaris, Serenitatis, Humboldtianum, and Crisium) were shown to possess central magnetic anomalies that could be accounted for by small quantities of metallic iron derived from the projectile.

As a result of vectorial magnetic field measurements made from orbit by the Lunar Prospector and Kaguya spacecraft, the global properties of the Moon's lithospheric magnetic field are now well characterized. The total magnetic field strength of the Moon at 30 km altitude from the model of Tsunakawa et al. (2015) is plotted in Figure 1, which is based on measurements from both missions. The nearside and farside hemispheres are plotted on the left and right, respectively, and the upper and lower set of images plot the field

strength using a linear and logarithmic color scale, respectively. As shown in the upper set of images, there are only a few dozen strong anomalies scattered across the lunar surface, and a large grouping of anomalies in the farside highlands. Though a few of these anomalies are associated with impact basins, the vast majority have no known correlation with any lunar geologic process. Many investigations have investigated the strength and direction of magnetization of the strongest and most isolated of these anomalies (e.g., Arkani-Hamed & Boutin, 2014; Blewett et al., 2007; Halekas et al., 2001, 2003; Hemingway & Garrick-Bethell, 2012; Hood, 2011; Hood et al., 2001, 2013; Mitchell et al., 2008; Nayak et al., 2017; Nicholas et al., 2007; Oliveira & Wieczorek, 2017; Oliveira et al., 2017; Purucker et al., 2012; Richmond et al., 2003, 2005; Takahashi et al., 2014; Wieczorek et al., 2012).

When the magnetic field strength is plotted using a linear scale, one could have the impression that only a small portion of the crust of the Moon was ever magnetized. However, when the field strength is plotted using a logarithmic scale, it is evident that magnetic fields are present everywhere and that large portions of the crust must in fact be magnetized. The lowest intensities plotted in this map are not a result of measurement noise as the same general tendencies can be seen in the surface field strengths derived from the Lunar Prospector electron reflectometer, which is based on a completely different measurement technique (see Mitchell et al., 2008). These weak, omnipresent crustal fields have not been investigated in any detail, and their origin is thus largely unexplored. In particular, it is not known if the magnetized materials responsible for these weak anomalies are located near the surface or if they are instead found deep in the crust. It is not known if the magnetic minerals are derived from endogenous lunar materials, or if they are instead a result of meteoritic contamination. Lastly, it is not known if these anomalies formed early in lunar history when the primordial crust was cooling, or if they formed later as a result of processes related to impact events or crustal magmatism. It is the origin of these weak fields that encompass the Moon that will be the main focus of this work.

To address the origin of lunar crustal magnetism, one would like to know the strength of magnetization in the crust, the geometry of the sources, and the depth range over which the sources reside. With this information, it would be possible to test various hypotheses. For example, if the magnetic sources were all located close to the surface, this might indicate that the sources were delivered to the Moon during impact events. If the sources were instead found deep in the crust, this might suggest that they either formed at the same time as the crust itself or they are related to later magmatic intrusions that cooled within the crust. Furthermore, if there were any variations in the strength of crustal magnetization, this could either be indicative of lateral variations in the abundance of magnetic carriers, or time variations in the strength of the field that magnetized the crust.

These questions will be addressed in this paper by the use of a statistical model of crustal magnetization. It will be assumed that crustal magnetization can be described by ensembles of magnetized sills or prisms, where the locations and magnetization vectors of the sources are both random. As will be shown, it is possible to derive analytic expressions for the power spectrum of the magnetic field that depend upon four parameters that describe the strength, size, and depth range of the magnetic sources. This model is highly inspired by a similar model that was developed by Voorhies (1998) and that was used to interpret the magnetic field of both Earth and Mars. In contrast to the pioneering work of Voorhies et al. (2002) and Voorhies (2008), who analyzed global magnetic power spectra, we will instead perform a localized power spectrum analysis using the techniques developed by Wieczorek and Simons (2005, 2007) to constrain how the model parameters vary across the surface of the Moon. A similar application of this approach applied to Mars can be found in Lewis and Simons (2012).

Our analysis comprises several steps. In section 2, the mathematical relations needed for a power spectrum analysis of a global magnetic field are provided. Two stochastic models of crustal magnetization are then developed that predict the global power spectrum, where one consists of ensembles of magnetized prisms and the other of magnetized sills. The properties of these two models are then explored and contrasted. In section 3, the technique of using a localized power spectrum analysis to invert for model parameters is described. This includes the construction of localization windows and a description of the manner by which both the data and model are localized. Furthermore, a Monte Carlo technique for placing confidence limits on the inversion parameters is described. In section 4, we perform a localized spectrum analysis of the Moon's magnetic field and invert for model parameters. Next, in section 5 we discuss two aspects of our model results. First, we describe how the size, geometry, and depth of sources constrain the origin and timing of crustal

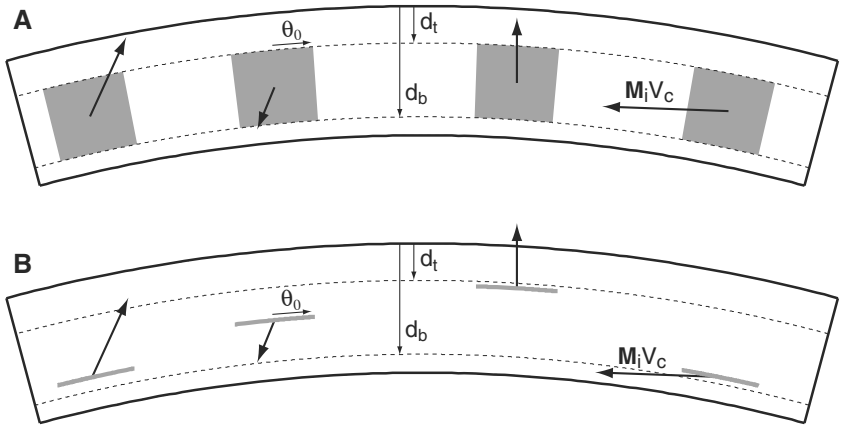

Figure 2. Schematic diagram of the stochastic model of crustal magnetization used in the magnetic field power spectrum analysis. (a) The magnetization is confined to a series of thick spherical prisms, each possessing the same volume V_c, the same angular radius θ_0, and the same depths to the top and bottom of magnetization, d_t and d_b, respectively. A spherical prism is here defined to be a cone with its apex at the center of the planet that is truncated by two spheres of different radii. The magnetization vectors $\mathbf{M}_i$ are random, as are the locations of each cap. (b) The magnetization is confined to a series of thin spherical caps with total magnetic moment $\mathbf{M}_i V_c$, and each cap is located randomly in the shell between the depths d_t and d_b.

magnetization. Second, we discuss the origin of a region of crust on the nearside that has extremely weak magnetization and field strengths. Finally, we conclude in section 6 by discussing some questions that remain unresolved and by providing guidance for future directions of research.

2. Stochastic Power Spectrum Models

The objective of this section is to calculate the theoretical power spectrum that results from a statistical collection of magnetized regions in a planetary body. This problem was studied previously by several authors. Voorhies, (1998, 2008) and Voorhies et al. (2002) gave expressions for the power spectrum when the magnetized regions were spatially uncorrelated dipoles in a spherical or ellipsoidal shell, depth correlated dipoles, or infinitesimally thin radially magnetized spherical caps. Jackson (1990, 1994) gave expressions for the case where the distribution of magnetization could be described by a lateral and vertical spatial correlation function. Bouligand et al. (2009) made use of a fractal model of magnetization whose Cartesian power spectrum was described by a power law in order to invert for the depth of magnetization on Earth. In a study by Thébault and Vervelidou (2015), the power spectrum of laterally varying magnetic susceptibility was assumed to follow a power law, which allowed to predict the magnetic power spectrum of the field induced by a central dipole. This technique was applied to Earth by Vervelidou and Thébault (2015) to invert for the thickness of the magnetic layer.

For the Moon, there are presently no fields generated by a core dynamo, and the observed static magnetic field is due entirely to magnetization in its lithosphere. To describe the observed magnetic power spectrum, two theoretical models will be developed that expand upon and generalize the results of Voorhies et al. (2002). The first model assumes that the power spectrum of the magnetic field can be approximated by that due to an ensemble of thick magnetized spherical prisms, each of which possesses a random lateral position, random volumetric magnetization, and random magnetization direction (model A in Figure 2). The fixed parameters of this model include the angular radius of the spherical prisms, a parameter that depends on the mean-squared dipole moment, and the depth to the top and bottom of the magnetized region. The second model is a generalization of the first and accounts for the case of thin magnetized caps (referred to below as sills) that are placed randomly within a thick spherical shell (model B in Figure 2). Both of these generic models are consistent with the functional forms given in Jackson (1994). Furthermore, these models reduce to the equations given in Voorhies et al. (2002) for their special cases of crustal magnetism. In particular, our model can account for their model of random dipoles placed within a finite thickness shell, vertically correlated dipoles within a finite thickness shell, and thin magnetized spherical caps. In contrast, we note that Voorhies et al. (2002) did not provide equations for vertically correlated spherical caps (our model A), nor uncorrelated spherical caps within a finite layer (our model B). Since the magnetic field of a uniformly magnetized sphere is equivalent

to that of a single dipole in the center of this sphere, our magnetic power spectrum models also account implicitly for uniformly magnetized spheres as well.

In the first subsection, definitions of the magnetic potential, power spectrum, and spherical harmonic normalizations are provided that are required for the analysis. The theoretical power spectrum is then derived for the two classes of magnetization that are shown in Figure 2. Following these derivations, the properties of their power spectra are described and compared.

2.1. Definitions

In the absence of free currents and time-variable electric fields, the curl of the magnetic field **B** is zero. This allows **B** to be expressed as the gradient of a scalar potential

$$\mathbf{B}(\mathbf{r}) = -\nabla U(\mathbf{r}) \tag{1}$$

that can be calculated explicitly via a surface and volume integral over the distribution of magnetization (e.g., Blakely, 1995, equation 5.4)

$$U(\mathbf{r}') = \frac{\mu_0}{4\pi}\int_S \frac{\mathbf{M}(\mathbf{r})\cdot \mathrm{d}\mathbf{a}}{|\mathbf{r}'-\mathbf{r}|} - \frac{\mu_0}{4\pi}\int_V \frac{\nabla\cdot\mathbf{M}(\mathbf{r})\,\mathrm{d}V}{|\mathbf{r}'-\mathbf{r}|}, \tag{2}$$

where **M** is the dipole moment per unit volume (in units of A m^{-1}) within the volume V enclosed by the surface S, d**a** is the differential surface area with direction normal to the surface, and μ_0 is the magnetic constant, $4\pi\times 10^{-7}$ T m A^{-1}. As a solution to Laplace's equation, the potential can be expanded exterior to the magnetized sources as a weighted sum of spherical harmonic functions

$$U(\mathbf{r}) = a\sum_{l=1}^{L}\sum_{m=-l}^{l}\left(\frac{a}{r}\right)^{l+1} g_{lm}\,Y_{lm}(\theta,\phi), \tag{3}$$

where Y_{lm} is a spherical harmonic function of degree l and order m as a function of colatitude θ and longitude ϕ, g_{lm} is the corresponding spherical harmonic Gauss coefficient (in units of teslas) evaluated at radius a, and L is the maximum spherical harmonic degree of the expansion. The real spherical harmonic functions are defined by

$$Y_{lm}(\theta,\phi) = \begin{cases} \bar{P}_{lm}(\cos\theta)\cos m\phi & \text{if } m \geq 0 \\ \bar{P}_{l|m|}(\cos\theta)\sin|m|\phi & \text{if } m < 0, \end{cases} \tag{4}$$

where the Schmidt seminormalized associated Legendre functions $\bar{P}_{lm}$ are related to the unnormalized functions, both of which exclude the Condon-Shortley phase of $(-1)^m$, by

$$\bar{P}_{lm}(x) = \sqrt{(2-\delta_{0m})\frac{(l-m)!}{(l+m)!}}\,P_{lm}(x), \tag{5}$$

where $x=\cos\theta$, and where δ is the Kronecker delta function. With these definitions, the spherical harmonics are orthogonal over the sphere and possess the normalization

$$\int_\Omega Y_{lm}(\theta,\phi)\,Y_{l'm'}(\theta,\phi)\,\mathrm{d}\Omega = \frac{4\pi}{(2l+1)}\,\delta_{ll'}\delta_{mm'}, \tag{6}$$

where $\mathrm{d}\Omega = \sin\theta\,\mathrm{d}\theta\,\mathrm{d}\phi$. If the coefficients g_{lm} are initially referenced to a radius a, as in equation (3), the corresponding coefficients referenced to a' can be shown to be given by

$$g_{lm}^{(a')} = g_{lm}\left(\frac{a}{a'}\right)^{l+2}. \tag{7}$$

Later, for the localized spectral analyses, it will be necessary to make use of 4π-normalized harmonics, which are defined by

$$\int_\Omega Y_{lm}^{(4\pi)}(\theta,\phi)\,Y_{l'm'}^{(4\pi)}(\theta,\phi)\,\mathrm{d}\Omega = 4\pi\,\delta_{ll'}\delta_{mm'}. \tag{8}$$

It is easily shown that Schmidt-seminormalized and 4π-normalized spherical harmonic coefficients are related by the expression

$$g_{lm}^{(4\pi)} = \frac{g_{lm}}{\sqrt{2l+1}}. \tag{9}$$

The total power of the magnetic potential at the reference radius a is

$$\frac{1}{4\pi}\int_{\Omega} U(a,\theta,\phi)^2\,\mathrm{d}\Omega = \sum_{l=1}^{L} S_U(l), \tag{10}$$

where the power spectrum S is

$$S_U(l) = \frac{a^2}{(2l+1)}\sum_{m=-l}^{l} g_{lm}^2 = a^2\sum_{m=-l}^{l}\left(g_{lm}^{(4\pi)}\right)^2. \tag{11}$$

Similarly, the total power of the magnetic field at radius r can be shown (after a somewhat complicated derivation) to be

$$\frac{1}{4\pi}\int_{\Omega} \mathbf{B}(\mathbf{r})\cdot\mathbf{B}(\mathbf{r})\,\mathrm{d}\Omega = \sum_{l=1}^{L} S_B(l,r), \tag{12}$$

where the Lowes-Mauersberger power spectrum of the magnetic intensity is (e.g., Lowes, 1966)

$$\begin{aligned} S_B(l,r) &= (a/r)^{2l+4}\,(l+1)\sum_{m=-l}^{l} g_{lm}^2, \\ &= (a/r)^{2l+4}\,(l+1)(2l+1)\,S_U(l)/a^2. \end{aligned} \tag{13}$$

For ease of notation, the radius at which the power spectrum is calculated will not be indicated when it is equal to the reference radius of the coefficients a. In the geomagnetism community, S_B is commonly denoted by the symbol R. If it is assumed that the coefficients g_{lm} are independent Gaussian random variables with zero mean, and that the variance of the coefficients depends only upon degree l, then it can be shown (see Wieczorek & Simons, 2007, appendix C) that the variances of the magnetic potential and magnetic power spectra are

$$\mathrm{var}\,\left\{S_U(l)\right\} = \frac{2}{(2l+1)}\langle S_U(l)\rangle^2, \tag{14}$$

$$\mathrm{var}\,\left\{S_B(l)\right\} = \frac{2}{(2l+1)}\langle S_B(l)\rangle^2, \tag{15}$$

where the operator $\langle\cdots\rangle$ denotes an ensemble average over the random variables.

2.2. Magnetized Prisms

We start by calculating the Gauss coefficients of a single uniformly magnetized spherical prism of angular radius θ_0 with upper and lower bounding radii r_+ and r_-, respectively (see Figure 2a). A spherical prism is here defined to be a cone with its apex at the center of the planet that is truncated by two spheres of different radii. For our inversions later in this paper, for convenience, the bounding radii will be expressed in terms of the depth to the top and bottom of the magnetized region, d_t and d_b, respectively. Since we are concerned primarily with calculating the power spectrum of the magnetic field, and since the power spectrum is invariant under a rotation of the coordinate system, with no loss of generality, we can place the center of the spherical cap at $\theta = 0$.

If the magnetization in the cap is constant in direction

$$\mathbf{M} = M_x\,\hat{\mathbf{x}} + M_y\,\hat{\mathbf{y}} + M_z\,\hat{\mathbf{z}}, \tag{16}$$

then both the divergence of $\mathbf{M}$ and the volume integral in equation (2) are identically zero. By calculating a surface integral over the prism, the Gauss coefficients can be shown to be equal to (see Appendix A)

$$\begin{aligned} g_{lm} =& \frac{\mu_0}{2}\left[\left(\frac{r_+}{a}\right)^{l+2} - \left(\frac{r_-}{a}\right)^{l+2}\right] \\ &\times\left[\frac{1}{2}\left(\delta_{m1}\,M_x + \delta_{m,-1}\,M_y\right)\left(\int_{\cos\theta_0}^{1}\bar{P}_{l1}(x)\bar{P}_{11}(x)\,\mathrm{d}x + \frac{\bar{P}_{l1}(\cos\theta_0)\sin\theta_0\cos\theta_0}{(l+2)}\right)\right. \\ &\left. +\ \delta_{m0}\,M_z\left(\int_{\cos\theta_0}^{1}\bar{P}_{l0}(x)\bar{P}_{10}(x)\,\mathrm{d}x - \frac{\bar{P}_{l0}(\cos\theta_0)\sin^2\theta_0}{(l+2)}\right)\right]. \end{aligned} \tag{17}$$

The coefficients for a magnetized spherical prism centered at any arbitrary location could be obtained using standard spherical harmonic rotation algorithms (e.g., Blanco et al., 1997; Varshalovich et al., 1988).

We next make the assumption that the planet contains N magnetized spherical prisms, all of the same size θ_0 and all with the same bounding radii r_+ and r_-. The Gauss coefficients for the ensemble of these prisms are simply

$$\tilde{g}_{lm} = \sum_{n=1}^{N} g_{lm}^{(n)} \tag{18}$$

where $g_{lm}^{(n)}$ are the coefficients of the nth prism centered at (θ_n, ϕ_n). If the position, volumetric magnetization, and magnetization direction of each prism are all random, the expectation of the power spectrum at radius a is

$$\langle S_B(l) \rangle = (l+1) \left\langle \sum_{m=-l}^{l} \sum_{i=1}^{N} \sum_{j=1}^{N} g_{lm}^{(i)} g_{lm}^{(j)} \right\rangle . \tag{19}$$

The expectation of the product of the two coefficients is zero when $i \neq j$, and since the power for an individual prism at degree l is unchanged by a rotation of coordinates, the power spectrum is simply N times the power of a single prism

$$\langle S_B(l) \rangle = N (l+1) \left\langle \sum_{m=-l}^{l} g_{lm}^{2} \right\rangle . \tag{20}$$

Given the assumption of random volumetric magnetizations and magnetization directions, we have

$$\langle M_x M_y \rangle = \langle M_x M_z \rangle = \langle M_y M_z \rangle = 0, \tag{21}$$

and

$$\langle M_x^2 \rangle = \langle M_y^2 \rangle = \langle M_z^2 \rangle = \langle M^2 \rangle / 3, \tag{22}$$

where $\langle M^2 \rangle$ is the average squared magnetization in the prisms. Using these equations to calculate the expectation of the square of equation (17), the expectation value of the power spectrum can be shown to be given by

$$\langle S_B(l) \rangle = N \langle M^2 \rangle Z_l^p \left(\theta_0, r_+, r_-, a \right), \tag{23}$$

where we have introduced for convenience the function Z^p that contains all terms related to the source geometry and volume, and where the superscript denotes that this is for the model of composed of prisms:

$$\begin{aligned} Z_l^p \left(\theta_0, r_+, r_-, a \right) = & \frac{\mu_0^2 (l+1)}{12} \left[\left(\frac{r_+}{a} \right)^{l+2} - \left(\frac{r_-}{a} \right)^{l+2} \right]^2 \\ & \times \left[\frac{1}{2} \left(\int_{\cos\theta_0}^{1} \bar{P}_{l1}(x) \bar{P}_{11}(x)\, dx + \frac{\bar{P}_{l1}(\cos\theta_0) \sin\theta_0 \cos\theta_0}{(l+2)} \right)^2 \right. \\ & \left. + \left(\int_{\cos\theta_0}^{1} \bar{P}_{l0}(x) \bar{P}_{10}(x)\, dx - \frac{\bar{P}_{l0}(\cos\theta_0) \sin^2\theta_0}{(l+2)} \right)^2 \right] . \end{aligned} \tag{24}$$

In practice, it will be more convenient to solve for a quantity related to the magnetic moment (in units of A m^2) as opposed to the magnetization M. This is because there will be a partial trade-off between the chosen magnetization and the volume of the magnetized region, with the volume dependence being accounted for in the function Z. Multiplying and dividing equation (23) by the volume-squared of the prism yields

$$\langle S_B(l) \rangle = N \langle M^2 \rangle V_p^2 \left\{ Z_l^p \left(\theta_0, r_+, r_-, a \right) \left(\frac{3}{2\pi (r_+^3 - r_-^3)(1 - \cos\theta_0)} \right)^2 \right\}, \tag{25}$$

where the volume of a single prism is given explicitly by

$$V_p = \frac{2\pi}{3}\left(r_+^3 - r_-^3\right)\left(1 - \cos\theta_0\right). \tag{26}$$

As shown in Appendix B, the integrals of the associated Legendre functions in equation (24) can be expressed in terms of the first derivatives of ordinary Legendre polynomials. Using the power spectrum for a prism of a specific size, it is straightforward to derive the predicted power spectrum for a given size-frequency distribution of prisms.

2.3. Magnetized Sills

A related model for the magnetic power spectrum of a planet is to assume that the observed spectrum is the result of many thin spherical caps that are each magnetized in a random direction and that are randomly distributed in the volume between radii r_+ and r_- (see Figure 2b). Such thin caps could be thought of as magmatic sills. We start by generalizing the power spectrum of N spherical prisms from equation (23) to that of a single thin cap at radius r_x with a finite, but small, thickness d. When r_+ and r_- approach r_x it is easily shown that

$$\begin{aligned}\langle S_B(l, r_x)\rangle =& \mu_0^2 \langle M^2\rangle \frac{(l+1)(l+2)^2}{12}\left(\frac{d}{a}\right)^2\left(\frac{r_x}{a}\right)^{2l+2} \\ &\times\left[\frac{1}{2}\left(\int_{\cos\theta_0}^{1}\bar{P}_{l1}(x)\bar{P}_{11}(x)\,\mathrm{d}x + \frac{\bar{P}_{l1}(\cos\theta_0)\sin\theta_0\cos\theta_0}{(l+2)}\right)^2\right. \\ &\left.+\left(\int_{\cos\theta_0}^{1}\bar{P}_{l0}(x)\bar{P}_{10}(x)\,\mathrm{d}x - \frac{\bar{P}_{l0}(\cos\theta_0)\sin^2\theta_0}{(l+2)}\right)^2\right].\end{aligned} \tag{27}$$

If N sills are located randomly within a volume V defined by upper and lower radii r_+ and r_-, such that the spatial density of sills is simply N/V, the total power spectrum can be calculated as

$$\langle S_B(l)\rangle = \frac{N}{V}\int_{r_-}^{r_+}\int_{\Omega} S_B(l, r_x)\, r_x^2\,\mathrm{d}r_x\,\mathrm{d}\Omega, \tag{28}$$

where

$$V = \frac{4\pi}{3}\left(r_+^3 - r_-^3\right). \tag{29}$$

At this point, two possible assumptions could be made about the sills: either the volume of the sills or the thickness of the sills could be considered constant. The two scenarios are nearly identical from a numerical point of view, but the constant thickness sill solution is more amenable to analysis when there is a distribution of sill sizes. Here we make the assumption that the sill thickness d is constant and present the results for constant volume sills in Appendix C. Integrating equation (28), the power spectrum is shown easily to be

$$\langle S_B(l)\rangle = N\langle M^2\rangle Z_l^s\left(\theta_0, r_+, r_-, a\right), \tag{30}$$

where

$$\begin{aligned}Z_l^s\left(\theta_0, r_+, r_-, a\right) =& \frac{\mu_0^2 d^2 a\pi}{3V}\frac{(l+1)(l+2)^2}{(2l+5)}\left[\left(\frac{r_+}{a}\right)^{2l+5} - \left(\frac{r_-}{a}\right)^{2l+5}\right] \\ &\times\left[\frac{1}{2}\left(\int_{\cos\theta_0}^{1}\bar{P}_{l1}(x)\bar{P}_{11}(x)\,\mathrm{d}x + \frac{\bar{P}_{l1}(\cos\theta_0)\sin\theta_0\cos\theta_0}{(l+2)}\right)^2\right. \\ &\left.+\left(\int_{\cos\theta_0}^{1}\bar{P}_{l0}(x)\bar{P}_{10}(x)\,\mathrm{d}x - \frac{\bar{P}_{l0}(\cos\theta_0)\sin^2\theta_0}{(l+2)}\right)^2\right],\end{aligned} \tag{31}$$

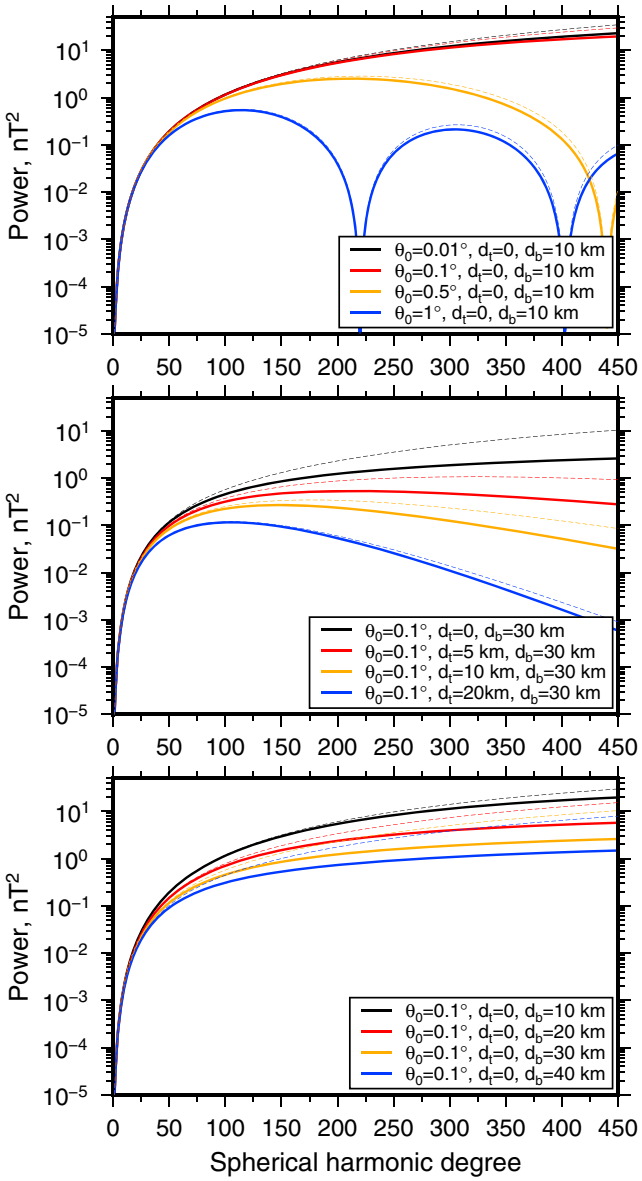

Figure 3. Example power spectra for ensembles of magnetized prisms (solid lines) and sills (thin dashed lines). (top) Dependence of the power spectrum on the angular radius θ_0 of the magnetized sources (1° is ~30 km on the lunar surface). All magnetized sources are placed between the surface and 10 km depth. (middle) Dependence of the power spectrum on the depth to the top of the magnetized region. The depth to the bottom of the magnetized region is 30 km, and θ_0 is 0.1°. (bottom) Dependence of the power spectrum on the depth to the bottom of the magnetized region. The top of the magnetized region is located at the surface and θ_0 is 0.1°.

and where the superscript s denotes that this is for the model composed of sills. Multiplying and dividing equation (30) by the volume squared of the sills yields

$$\langle S_B(l)\rangle = N\langle M^2\rangle V_s^2 \left\{ Z_l^s\left(\theta_0, r_+, r_-, a\right)\left(\frac{5\left(r_+^3 - r_-^3\right)}{6\,\pi\, d\left(r_+^5 - r_-^5\right)(1-\cos\theta_0)}\right)^2\right\}, \tag{32}$$

where the average volume of a sill of constant thickness and angular radius θ_0 is

$$V_s = \frac{6\,\pi\, d}{5}\frac{\left(r_+^5 - r_-^5\right)}{\left(r_+^3 - r_-^3\right)}(1-\cos\theta_0). \tag{33}$$

It is noted that the last term in brackets of equation (32) does not depend upon the sill thickness d, as the reciprocal of d^{-2} is found in the function Z^s.

2.4. Example Power Spectra

The model power spectra for randomly magnetized prisms and sills are very similar in form. As seen in equations (25) and (32), the spectra depend upon a multiplicative prefactor $N\langle M^2\rangle V^2$ that is the total number of sources multiplied by their mean-squared dipole moment, and a degree-dependent term Z that depends upon the geometry of the sources. The geometric function Z is composed further of two multiplicative terms, one that depends solely on the radii over which the sources reside and another that depends solely on the angular size of the sources. Given the nature of the prefactor $N\langle M^2\rangle V^2$, it will not be possible to invert individually for the number of sources, their magnetization, or their dipole moment, as they are all correlated.

The three terms that control the form of the geometric factor Z are the depth to the top of the magnetized region d_t, the depth to the bottom of the magnetized region d_b, and the angular radius of the sources θ_0. The dependence of the model spectrum on these terms is illustrated in Figure 3, where the top panel shows how the magnetic power spectrum varies as a function of the angular size of the sources, the middle panel shows how the spectra vary as a function of the depth to the top of the magnetized region, and the bottom panel shows the dependence on the depth to the bottom of the magnetized region. The maximum spherical harmonic degree plotted is 450, which corresponds to the maximum resolution of the lunar magnetic field that will be employed later.

In Figure 3 (top), spectra are plotted for several values of θ_0 from 0.01° (~30 m) to 1° (~30 km), with d_t and d_b set to constant values of 0 and 10 km, respectively. It is first noted that the model spectra for magnetized sills and prisms are nearly identical for degrees less than about 150. For higher degrees, the power is slightly larger for magnetized sills than for magnetized prisms. For both models, the majority of the power is found to reside in the first spectral lobe, which empirically is found to have a bandwidth of about $1.2\times180/\theta_0$, with θ_0 in degrees. The spectral lobes are a result of the fact that the magnetized regions have a finite width with sharp boundaries. Each successive lobe has a lower maximum amplitude, and for the smallest values of θ_0 plotted (0.01° and 0.1°), only a portion of the first lobe is visible. As θ_0 approaches zero, the spectra are seen to converge rapidly to an asymptotic form.

In Figure 3 (middle), spectra are plotted for several values of the depth to the top of the magnetized region, from 0 to 20 km. Here the depth to the bottom of the sources was set to 30 km, which is slightly smaller than the average thickness of the lunar crust (e.g., Wieczorek et al., 2013), and the angular radius of the sources was set to 0.1°. The depth to the top of the sources is seen to have a major influence on the spectra at the

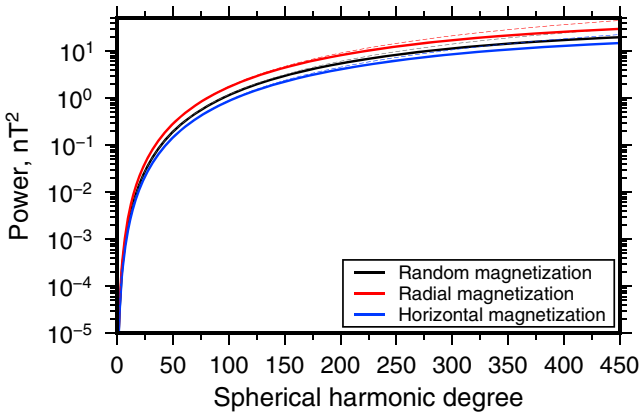

Figure 4. Dependence of the magnetic power spectrum on the direction of magnetization for ensembles of prisms (solid lines) and sills (thin dashed lines). Black curves correspond to the case where the magnetization directions are random, whereas the red and blue curves correspond to the cases where the sources are all magnetized in either the radial or horizontal directions, respectively. All magnetized sources are placed between the surface and 10 km depth, and the angular radius θ_0 of the sources is 0.1°.

highest degrees. As the depth to the top of the sources increases, the high-degree power decreases. This behavior is easily understood from the mathematical form of the geometric function Z in equations (24) and (31), and suggests that this value will be constrained easily from observations.

Figure 3 (bottom) demonstrates how the magnetic power spectrum depends upon the depth to the bottom of the magnetized sources. In this example, the angular radius of the sources was set to 0.1°, the top of the magnetic sources was set to the surface, and the depth of the sources was varied from 10 to 40 km. For most of the degree range that is plotted, the spectra all have somewhat similar slopes, especially for degrees greater than about 100. Beyond this degree, the spectra are approximately offset only by a vertical scaling factor. This behavior suggest that it will be difficult to invert for the depth to the bottom of the magnetized region as this will partially trade off with the factor $N\langle M^2\rangle V^2$ that multiplies each of these curves.

Finally, we consider how the direction of magnetization affects the model power spectra. Up until this point, we have treated the case where the direction of magnetization of each individual source was random. This assumption provided a simple expression for the expectation of the magnetization vector in each orthogonal direction as given by equation (22), as well as zero values for the cross expectation of two components in equation (21). An alternative model might be to instead assume that all magnetic sources were magnetized in the same direction. We quantify how the magnetic power spectrum for this case differs from that of random magnetization by considering two end-member cases: horizontally magnetized sources and radially magnetized sources.

The derivations for these models are nearly identical to those presented earlier in this section, and only differ by setting $\mathbf{M} = M_x\,\hat{\mathbf{x}}$ for horizontally magnetized sources and $\mathbf{M} = M_z\,\hat{\mathbf{z}}$ for vertically magnetized sources. In Figure 4 we plot these two models in blue and red, respectively. The power spectrum for the case of radially magnetized sources is found to be always about 2 times larger than the case of horizontally magnetized sources. As these two curves are very similar to our model with random magnetization directions, which lies between the two end-members, we do not expect the results of our inversion to depend sensitively on the actual direction of magnetization. This factor of 2 difference will simply become incorporated into the prefactor $N\langle M^2\rangle V^2$.

3. Localized Spectrum Analysis

A stochastic model consisting of randomly magnetized prisms or sills was developed in section 2 that predicts the expected global magnetic power spectrum of a planet. This model assumes implicitly that the properties of the magnetic sources are globally uniform and do not vary from place to place. In reality, as a result of lateral variations in geologic processes (such as variations in crustal cooling rates and variations in the abundance of the magnetic carriers), one might expect that the model parameters should also vary as a function of position. To quantify such lateral variations, instead of inverting the observed global magnetic power spectrum for best fitting model parameters, we will perform a localized multitaper power spectrum analysis that extracts the spectral properties of the magnetic field over prescribed regions. In this section, we describe the methodology used in this analysis, which includes the construction of a global spherical harmonic model of the Moon's magnetic field based on the gridded data of Tsunakawa et al. (2015), the construction of spatiospectral localization windows for the multitaper spectrum analyses, the inversion of the localized spectra for model parameters, and Monte Carlo techniques for estimating the uncertainties of the model parameters.

We first develop a global spherical harmonic model of the Moon's magnetic field that is based on the global 0.2° gridded map of the radial component of the magnetic field developed by Tsunakawa et al. (2015). This model is based on a combination of vector magnetic field measurements from the Kaguya and Lunar Prospector spacecraft, and after a global model for the radial field was constructed, Tsunakawa et al. (2015) were able to derive maps of the other two horizontal components directly from their radial field map. The gridded model of the radial field thus contains all the information in their model. Using the software package SHTOOLS (Wieczorek et al., 2016), the spherical harmonic coefficients of the radial magnetic field were calculated,

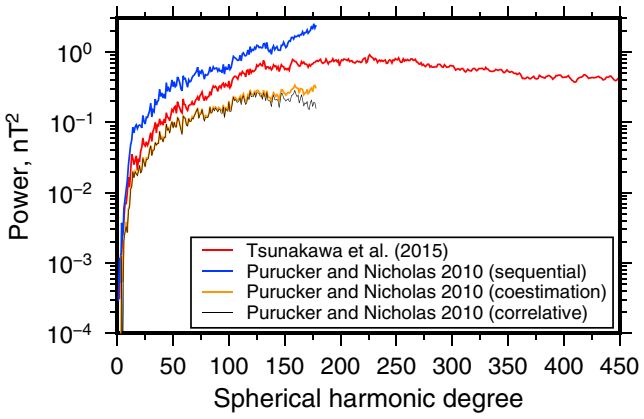

Figure 5. Magnetic power spectra of the Moon. The power spectrum of the model developed by Tsunakawa et al. (2015) is based on measurements obtained by the Kaguya and Lunar Prospector spacecraft, whereas the three models of Purucker and Nicholas (2010) are based exclusively on measurements from Lunar Prospector. The power is calculated at a radius of 1,737.4 km.

and the Gauss coefficients of the magnetic potential were then obtained by dividing these by $(l + 1)$ (cf. equation (3). The final spherical harmonic model is developed up to degree 449, which is the maximum degree allowed by the Driscoll and Healy (1994) sampling theorem.

The magnetic field intensity of the Tsunakawa et al. (2015) model was shown previously in map form in Figure 1, and here we plot in Figure 5 the magnetic power spectrum of this model. The form of the power spectrum is similar in many respects to that of the model spectrum developed in section 2. The power is low at the lowest degrees and then increases several orders of magnitude over the first 100 degrees. The power then increases more slowly to achieve a broad peak close to degree 200 and then decreases slightly and continues with a nearly constant value after about degree 350. Also plotted are the power spectra of three different global models developed by Purucker and Nicholas (2010) that were based solely on Lunar Prospector data. These models have a lower spatial resolution than the Tsunakawa et al. (2015) model, with a maximum spherical harmonic degree of 180. Furthermore, it is seen that the power spectra of the three Purucker and Nicholas (2010) models differ by about a factor of 5, which they interpreted to be a result of the strong regularization applied to their "coestimation" model. The power spectrum of the Tsunakawa et al. (2015) model lies about halfway between the "sequential" and "coestimation" models of Purucker and Nicholas (2010).

To obtain estimates of the magnetic power spectrum localized to a prescribed region of interest, we use the multitaper spectrum analysis technique as developed in spherical geometry for scalar fields by Wieczorek and Simons (2005, 2007). The technique is conceptually very simple: Several orthogonal windows of prescribed spherical harmonic bandwidth are constructed that localize optimally their energy in a spherical cap of specified angular radius, the localization window is rotated to the region of interest, the data are multiplied by the window, the resulting function is expanded in spherical harmonics, and the power spectrum of the localized function is computed. The multitaper spectrum estimate is defined as the average of the spectra from each of the individual localization windows. By using several orthogonal localization windows, statistical fluctuations associated with the underlying process are reduced, which provides a better estimate of the power spectrum expectation of the process. The uncertainty in the multitaper spectrum estimates decreases as $1/\sqrt{K}$, where K is the number of localization windows (Wieczorek & Simons, 2007, equation 4.4). All of these computations are readily performed by routines in the SHTOOLS software package.

Only minor modifications to this method are required when applying a multitaper spectrum analysis to magnetic field data (see also Lewis & Simons, 2012). First, we convert the Schmidt seminormalized Gauss coefficients to 4π-normalized coefficients using equation (9) in order to be compatible with the normalization used by the localization windows. Second, we localize the magnetic potential (not the vector components) and then convert the localized spectrum of the potential to a localized power spectrum of the magnetic field by multiplying by $(2l + 1)(l + 1)/a^2$ (see equation (13)). At this point, all that is left to do is to choose the size and the spectral bandwidth L_{win} of the window: these two quantities determine how many windows will be well localized. We note that it is desirable that the spectral bandwidth of the windows be as small as possible, since the localized spectrum can be interpreted only between L_{win} and $L - L_{\text{win}}$, where L is here 449. On the low-degree end, this limitation is a result of the fact that it is not possible to resolve wavelengths that are greater than the size of the localization region. On the high-degree end, this limitation arises because the localized spectrum at degrees greater than $L - L_{\text{win}}$ depends upon global spherical harmonic model coefficients beyond what are available. As L_{win} increases, the number of windows that are well localized increases, the uncertainty associated with the multitaper spectrum estimate decreases, and the degree range over which the localized power spectrum can be interpreted decreases. Alternative localization techniques that make use of vectorial fields can be found in Thébault et al. (2006) and Plattner and Simons (2017).

As an illustrative example, we chose the size of the localization region to be a spherical cap with an angular radius of 10° and then chose the spectral bandwidth of the windows to be 26, 35, 46, and 60. Using the criteria that a window is well localized if 99% of its power is concentrated in the region of interest, these bandwidths provide 1, 3, 6, and 12 windows that are well localized. Figure 6 plots the localized magnetic power spectra

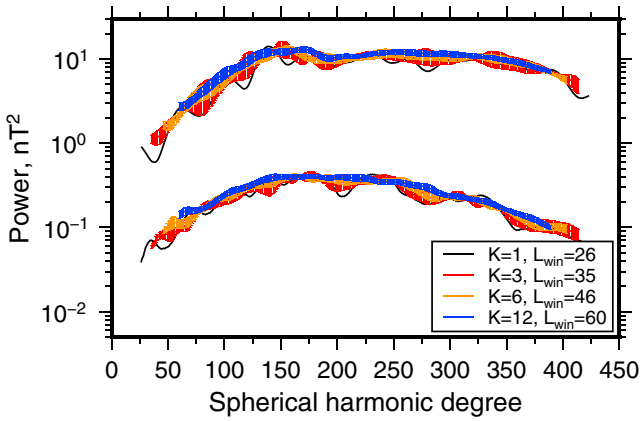

Figure 6. Example localized magnetic power spectra using windows with an angular radius of 10°. The localized spectra were calculated over two representative regions on the farside: a high field strength region at (30°S, 170°E) and a medium field strength region at (15°S, 120°E). The number of well-localized tapers K for the specified spectral bandwidth of the window varies from 1 to 12 and the plotted error bars correspond to the standard error of the multitaper estimate.

using these four sets of windows for two regions on the farside of the Moon, one that has high field strengths in the northern portion of the South Pole-Aitken basin and another with low field strengths to the northwest of this basin. The spectra of the two regions are similar in form and differ primarily by a multiplicative constant, reflecting different strengths of magnetization in the crust. As is seen, when a single localization window is used (black lines), the spectrum possesses substantial oscillations, but as more and more windows are employed, the multitaper spectrum estimate becomes progressively smoother. The uncertainty of the spectral estimates decreases with the number of windows, and as expected, the uncertainty using 12 windows is about 2 times smaller than when using 3 windows. As the number of well-localized windows increases, the bandwidth of the windows also increases, which reduces the range of spherical harmonic degrees that can be interpreted.

When a global function is multiplied by a localization window, the power spectrum of the localized function will differ naturally from that of the global function. Thus, when comparing localized spectra of the observed magnetic field to a model, it is important that these be compared to models that are localized in a similar manner. In many geophysical analyses, such as when analyzing the relation between gravity and topography (e.g., Besserer et al., 2014), it is possible to construct a forward model of the field that is then localized in exactly the same manner as the data. In our case, though, the magnetization model is inherently statistical in nature, and the generation of individual forward models would be somewhat more cumbersome. Fortunately, a relationship does exist that relates the statistical expectation of the localized multitaper spectrum estimate to the power spectra of the global field and window (Wieczorek & Simons, 2005, 2007). In particular, for a global scalar function f and a set of localization windows $h^{(k)}$, the expectation of the multitaper power spectrum of the localized field Φ is

$$\left\langle S_{\Phi\Phi}^{(mt)}(l) \right\rangle = \sum_{j=0}^{L_{\mathrm{win}}} \left(\sum_{k=1}^{K} a_k \, S_{hh}^{(k)}(j) \right) \sum_{i=|l-j|}^{l+j} S_{ff}(i) \left(C_{j0i0}^{l0} \right)^2 , \tag{34}$$

where the symbol C is a Clebsch-Gordan coefficient, S_{hh} and S_{ff} are respectively the power spectrum of the window h and function f, and a_k are the weights used in constructing the multitaper estimate. For this study, a_k will be set equal to $1/K$. The derivation of this equation makes only the assumption that the spherical harmonic coefficients of the function f are zero-mean random variables, and that the coefficients are isotropic, with the variance depending solely on spherical harmonic degree.

When inverting the observed localized magnetic power spectra for model parameters, the goodness of fit between the observations and model will be quantified by a reduced χ^2 function. This misfit function depends upon the four parameters of our model, $N\langle M^2 \rangle V^2$, d_t, d_b, and θ_0, and is given explicitly by

$$\chi_\nu^2 \left(N\langle M^2 \rangle V^2, d_t, d_b, \theta_0 \right) = \frac{1}{\nu} \sum_{l=L_{\mathrm{win}}}^{L-L_{\mathrm{win}}} \left(\frac{S_B^{(mt)}(l) - S_B^{(\mathrm{mt})} \left(l; N\langle M^2 \rangle V^2, d_t, d_b, \theta_0 \right)}{\sigma^{(\mathrm{mt})}(l)} \right)^2 , \tag{35}$$

where ν is the number of degrees of freedom that is equal to $L - 2L_{\mathrm{win}} - 4$, the first two terms in the numerator are respectively the observed multitaper power spectrum and the localized version of the model calculated from equation (34), and $\sigma^{(\mathrm{mt})}$ is the uncertainty associated with the observed multitaper power spectrum, which is simply the standard error of the K windowed power spectra. The best fitting model parameters will be obtained by sampling the entire model space using an exhaustive grid search.

The 1σ uncertainties on the inversion parameters will be estimated by using a criterion for the maximum allowable misfit that comes from Monte Carlo simulations. To determine this maximum allowable misfit, a global model power spectrum of the magnetic potential is first calculated that corresponds to a set of representative model parameters. Tests using different model parameters show that the final uncertainties are insensitive to the exact values chosen. Assuming that the spherical harmonic coefficients of the magnetic potential are random variables, which is consistent with the assumptions of our stochastic model, the Gauss coefficients were set to Gaussian random deviates with variance given by equation (14). By definition, this

ensures that the expectation of the magnetic power spectrum is equal to that of the global model. Next, a localized analysis is performed on the simulated Gauss coefficients, and the best fitting model parameters are determined by minimizing the χ^2_v function of equation (35). The best fitting χ^2_v is saved, and the entire procedure is repeated using a new set of Gaussian deviates for the coefficients of the magnetic potential. The cumulative probability distribution $P(\chi^2_v)$ is computed, and the value of χ^2_v where $P(\chi^2_v)$ is equal to 68.2% is ultimately used as the maximum allowable misfit . This misfit defines the 68.2% confidence intervals for the inversion parameters, which determines the 1-σ uncertainties with respect to the best fitting value.

4. Results

A localized spectral analysis and inversion for model parameters was performed at each point on an equally spaced grid that covered the lunar surface with a 5° grid spacing at the equator. At each location, the magnetic potential coefficients were downward continued to the mean elevation of the analysis region using the global topographic map of Smith et al. (2010), and the depths to the top and bottom of the magnetized region were referenced to this datum. The localization analyses made use of windows with an angular radii of 8° (a diameter of about 480 km) and spectral bandwidths of 58, which yielded six well-localized windows. The localized spectrum was analyzed from degree 58 to 391, and the misfit was calculated by an exhaustive grid search of the four-parameter model space. As will be discussed at the end of this section, the results were found to be insensitive to variations in the degree range of the localized spectrum that was analyzed and to variations in the localization window parameters.

We start by discussing the inversion results using the magnetic power spectrum model that consists of magnetized sills (the results of the model using prisms are very similar). In Figure 7 are plotted from top to bottom the results for the square root of $N\langle M^2\rangle V^2$, the depth to the top of the magnetized region, the depth to the bottom of the magnetized region, and the sill radius. From left to right are plotted the best fitting values interpolated over the entire surface, and the 1σ lower and upper limits of the model parameters. For the uncertainties, individual points are plotted only when the misfit is below the maximum value expected for the 68% confidence limit. As expected, about 74% of the analyses can be fit by the model to within the 68% confidence limit.

The results for the square root of the parameter $N\langle M^2\rangle V^2$ (in units of A m^2) are perhaps the easiest to interpret. This parameter is a measure of the number of magnetized sills in the crust, their magnetization, and the sill volume. The best fitting values for this parameter vary over about 3 orders of magnitude, and the lateral variations in this parameter are broadly similar to those seen in the observed magnetic field intensity as plotted in the lower portion of Figure 1. Magnetic field strength is thus, unsurprisingly, largely correlated with the number of magnetized sills in the crust, and/or their magnetization. As seen in this map, there are two regions that have exceedingly weak magnetizations: one prominent region on the nearside in the region of the Imbrium basin and Oceanus Procellarum and a second smaller region on the northern farside highlands. Each of these regions has prominent magnetic lows in the total magnetic intensity. This map also shows that some of strongest regions of magnetization are located in the central farside highlands, just north of the South Pole-Aitken basin. This again correlates well with the regions having the strongest magnetic field intensities in Figure 1. Maps of the 1σ limits of this parameter show the same behavior as the best fitting values.

The next best constrained parameter is the depth to the top of the magnetized region. It is first noted that even though this depth was allowed to lie above the surface in our inversions, the best fitting depths of magnetization lie almost always below the surface. This is a positive outcome of the model and lends credibility to the assumptions under which it was generated. (It is noted that the depth of magnetization in a study of Mars by Lewis and Simons (2012) was sometimes found to lie above the surface.) Though a few regions do predict best fitting depths of magnetization above the surface, within uncertainties, these regions are consistent with having the top of the magnetized zone located at the surface or below. A histogram of the best fitting depths are plotted in Figure 8, which shows that the depth to the top of the magnetized region lies between the surface and about 25 km depth. The average depth to the top of the magnetized region is 11 km, and the average uncertainties on the depths are ±6 km. Thus, though some magnetization extends to the surface, in other regions it is below the surface by more than 10 km.

The spatial distribution of the depth to the top of magnetization is heterogeneous, and it is not easy to correlate with known geologic processes. Nevertheless, it is noted that there is a broad region on the farside that possesses extremely shallow depths of magnetization. This region encompasses a portion of the South Pole-Aitken basin near (180°E, 45°S) and extends to both the northwest and northeast in a V-shaped pattern.

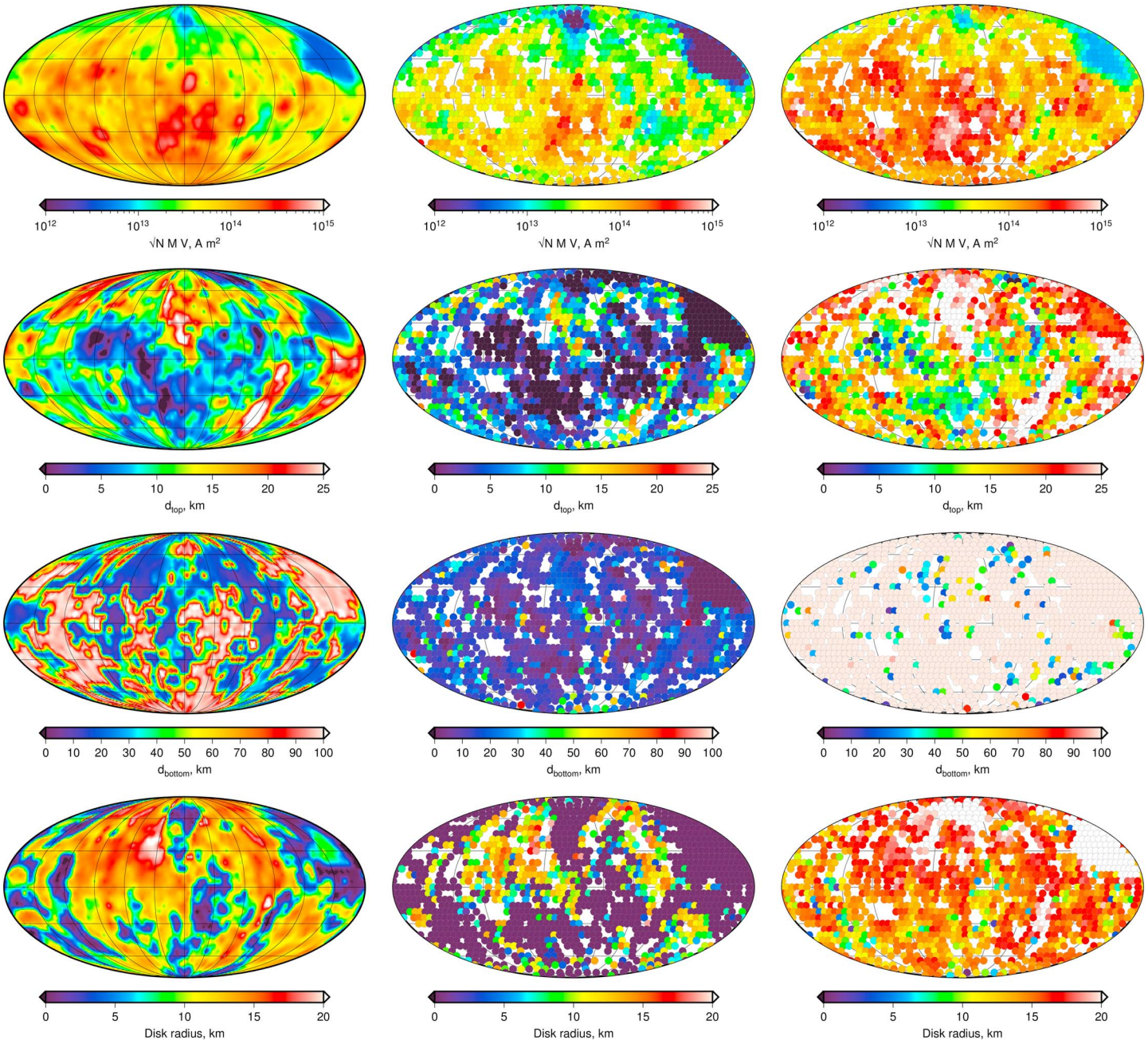

Figure 7. Inversion results for ensembles of magnetized sills. From top to bottom are global maps centered on the farside of the square root of $N\langle M^2\rangle V^2$, depth to the top of the magnetized region, depth to the bottom of the magnetized region, and sill radius. From left to right are shown interpolated best fitting parameters and the 1σ lower and upper limits for each analysis. For the upper and lower limits, data points are plotted only if the minimum misfit is below the expected 68% limit from Monte Carlo simulations. The angular radius of the localization windows is 8° , the window bandwidth is 58, and the number of localization windows used is six. Analyses were performed on an equally spaced grid with a spacing of 5° at the equator, and data are presented in Mollweide projections centered on the 180° meridian. Grid lines are spaced every 30° in latitude and longitude.

For this region, the best fitting depths range from about 0 to 7 km, the shallower 1σ limit approaches the surface (black circles), and the deeper 1σ limit is close to 10 km. The depth to the top of magnetization in this region is thus shallow. The region of low field intensities on the nearside also possesses shallow depths to the top of magnetization, but the shallower 1σ limits are here close to 20 km. Outside of these regions, the shallowest 1σ limits of the depths to the top of the magnetized regions are several kilometers below the surface (i.e., those regions with non-black circles in the middle panel), suggesting that the upper portion of the crust is there not magnetized.

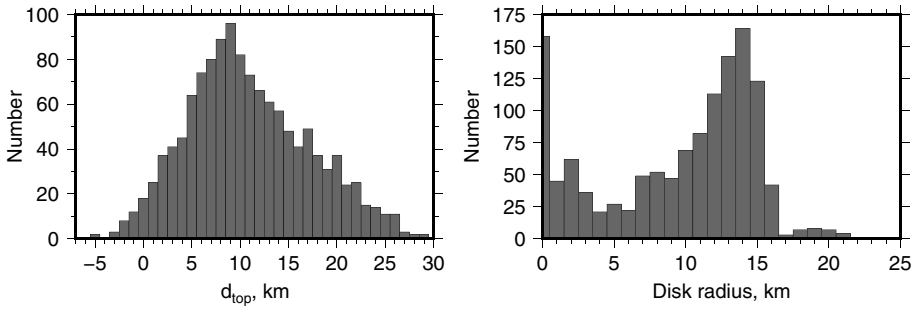

Figure 8. Histograms of the best fitting depths to the top of the (left) magnetized region and (right) sill radii.

In contrast to the depth to the top of the magnetized region, the depth to the bottom of this region is not well constrained, if at all. Though there are regional variations in the best fitting depths to the bottom of the magnetized region, the 1σ lower limits extend to 100 km, which was the maximum value tested in our inversions. It was noted previously in section 2.4 that the form of the theoretical power spectrum would make it difficult to constrain this parameter.

Lastly, our inversions place some constraints on the angular radius of the sills in our model. A histogram of the sill radii is plotted in Figure 8 showing that the radii are almost all less than about 15 km. This distribution is somewhat bimodal, with peaks near 0 and 13 km, but as shown in Figure 7, the uncertainties on this parameter are somewhat large. The vast majority of our analyses have 1σ lower limits on the sill radii that approach 0 km, and the 1σ upper limits approach 20 km. There are some regions, however, as shown by the colored circles in Figure 7 (middle column), that appear to constrain the sill radii to larger values close to 15 km. It is noted that the maximum disk radii of about 20 km in our inversions is likely related to the spatial resolution of the magnetic field model of Tsunakawa et al. (2015). As shown in section 2.4, the majority of the model power is confined to lie within the first spectral lobe of bandwidth $1.2 \times 180/\theta_0$. Since this spectral lobe is never completely resolved in the localized spectra, the disk radii must be less than about 15 km. A higher-resolution model of the magnetic field would help to further constrain this value.

In addition to inverting for model parameters using the model of magnetized sills, inversions were also performed using magnetized prisms. The two models fit the observations equally well, and the results are quite similar. The only difference worth noting is that the depths to the top of the magnetized region are often shallower by up to 6 km when compared to the model of magnetized sills. As a result of this, those regions with near-zero depths of magnetization in Figure 7 predict magnetization to lie above the surface. The reason for this behavior can be seen in Figure 3, which shows that the power in the high-degree portion of the spectrum is slightly greater for the model of magnetized sills than prisms. In our inversions with magnetized prisms, this is compensated by decreasing the depth to the top of the magnetized region, which increases the power at these degrees. Even though it is unphysical to have magnetization lying above the surface, we cannot exclude the prism model given the uncertainties on this inversion parameter. For our simulations using sills with localization windows of 10°, out of 412 analyses, 6 analysis regions have best fitting magnetization depths above the surface. Nevertheless, within 1σ uncertainties, all of these are consistent with the magnetization being located below the surface. For the prism model, 54 analysis regions have best fitting depths above the surface, and 47 of these are consistent with lying below the surface within 1σ uncertainties. If it were possible to decrease the uncertainties on the depth to the top of magnetization (which is about $\pm 6-8$ km), it might be possible to distinguish between these two models. The results for the sill model will be used in our discussion, but none of the conclusions would differ if the prism model were used instead.

The sensitivity of our results to the parameters of our inversion was tested in several ways. First, as the highest degrees of the magnetic field could perhaps be contaminated by noise, the degree range over which the model was compared to the observations was first varied, by truncating the global model at spherical harmonic degrees 250 and 350. The major consequence of using lower maximum degrees was to have higher uncertainties on the inverted model parameters. The results for the square root of $N\langle M^2\rangle V^2$ and the depth to the bottom of the magnetized region were unchanged by using the lower degree ranges. As the inverted degree range decreased, however, the shallower 1σ limits on the depth to the top of the magnetized regions also increased, such that a larger portion of the analyses were compatible with having the magnetized region

extending to the surface. In contrast, the deeper 1σ limit did not change much. As expected, the range of sill radii increased as the maximum spatial resolution of the model was degraded.

The sensitivity of our inversion results to the size of the localization windows was also tested. Inversions were performed using localization windows with angular radii of 8, 9, 10, 12, and 16°, all with spectral bandwidths of 50. For these parameters, there were respectively 3, 5, 6, 12, and 25 orthogonal well-localized windows for computing the multitaper spectrum. For our inversions using the full resolution of the global model, the best fitting parameters and 1σ limits were largely unchanged. Though the uncertainties were somewhat greater for the inversions with smaller window sizes, this effect was not nearly as dramatic as truncating the global model to lower degrees. As the window size decreased, the lateral variability in the best fitting model parameters increased somewhat. Six orthogonal localization windows with a size of 8° were chosen subjectively to present our nominal results as it was visually smooth and largely devoid of statistical fluctuations. The conclusions of this work would not be affected if they were based on the results using either larger or smaller localization windows.

5. Discussion

5.1. Origin and Timing of Crustal Magnetization

The results of our analysis place constraints on the strength, depth, and geometry of magnetic sources in the lunar crust, and this allows us to investigate not only the origin of lunar magnetic materials but also the timing of when they became magnetized. One of the first results concerns the size and thickness of the regions that are magnetized in the crust. Our inversions imply that the horizontal scale of magnetization is less than about 30 km, but given that this upper limit is likely related to the maximum spatial resolution of the magnetic field model, it is plausible that the width of the magnetized regions could be even smaller. Thus, as opposed to having wide coherent blocks of materials that are magnetized, the picture that emerges for the Moon is rather a scenario where the magnetization is confined to numerous small regions.

The range of depths where the magnetized sills in our model reside is well constrained. As shown in Figure 8, the depths to the top of the magnetized region vary laterally and extend from the surface down to about 25 km. When considering the shallower 1σ uncertainty on this parameter, the depths to the top of the magnetized region must be deeper than more than several kilometers for over more than half of the Moon's surface. In contrast to the depth to the top of the magnetized region, the depth to the bottom of this region is relatively unconstrained with the 1σ limits extending to more than 100 km. One might expect that the maximum depth to the bottom of the magnetized region would correspond to the crust-mantle interface. Inversions of both Gravity Recovery and Interior Laboratory (GRAIL) gravity and Apollo seismic data suggest that the average thickness of the crust lies somewhere between 34 and 43 km, and that locally, the thickness can be as great as 80 km Wieczorek et al. (2013). Together, these observations imply that much of the deep crust of the Moon (deeper than 10 km) is magnetized, and that in some places the magnetization extends to the surface. The upper 10 km or so of the crust is unmagnetized in places, suggesting that either the upper crust was never magnetized in these regions or the upper crust was subsequently demagnetized, such as by later impact events.

The depth range, lateral size of the magnetized regions, and distribution of magnetization place important constraints on the origin of the magnetic carriers. Three possibilities that can be considered are that (1) the magnetization is related to magmatic intrusions in the crust, (2) the magnetization is related to materials accreted to the Moon during large impacts, and (3) the magnetization is primordial and formed at the same time as the crust. The first scenario involving magmatic intrusions can be safely ruled out. Though the size of the magnetized regions is consistent with what one might expect for magmatic sills, nearly the entire crust of the Moon possesses significant magnetization from the perspective of the parameter $N\langle M^2\rangle V^2$. The vast majority of this crust resides in the lunar highlands where there are few basaltic eruptions and where there is little remote sensing evidence for basaltic intrusions in the largely anorthositic crust. In fact, the vast majority of lavas that erupted on the Moon are located on the nearside in Oceanus Procellarum and Mare Imbrium, and it is this region that has the lowest magnetic field intensities. Magmatic intrusions might account for a few isolated magnetic anomalies in the highlands, but not the majority of the ubiquitous weak fields that are found there.

The second possibility for the origin of the magnetic carriers is that they were delivered to the Moon during large impact events. For this scenario, one might expect that the magnetization would be shallowest within and surrounding the largest basins. The depth to the top of the magnetized region is replotted in Figure 9

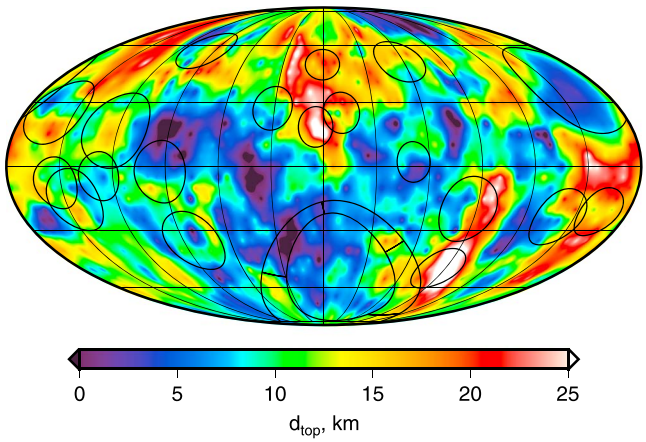

Figure 9. Impact basins with sizes greater than 500 km diameter superposed on the depth to the top of magnetization. Basin sizes and locations are from Neumann et al. (2015), with the exception of the South Pole-Aitken basin where both the inner basin floor and outer structural rim of Garrick-Bethell and Zuber (2009) are plotted. Data are presented in a Mollweide projection centered on the 180° meridian. Grid lines are spaced every 30° in latitude and longitude.

along with the sizes of all impact basins that are greater than 500 km in diameter. Though there are few obvious correlations between impact basins and the depth of magnetization, two possible exceptions are the 1,321 km diameter Imbrium basin centered at (37°N, 18.5°W) and the 2,400 km diameter South Pole-Aitken basin centered at (53°S, 191°W). For the Imbrium basin, the best fitting depth to the top of the magnetized region is only a few kilometers, with 1σ uncertainties extending from the surface to about 20 km. A plausible but equivocal interpretation is that the shallow depths of magnetization here are related to iron-rich materials derived from the impactor that were deposited in the basin center. The interior of the South Pole-Aitken basin is also associated with best fitting depths to the top of magnetization that are only a few kilometers. Furthermore, these shallow depths appear to extend to both the northwest and northeast of this basin in a broad V-shaped pattern. The 1σ limits for these depths are also shallow, extending from the surface to about 10 km depth. The shallow magnetization in this region of the Moon is plausibly attributed to iron-rich materials derived from the projectile that formed this basin, as originally proposed by Wieczorek et al. (2012). The northwest and northeast extensions of this material are consistent with projectile materials being deposited in the downrange direction of a south to north oblique impact Garrick-Bethell and Zuber (2009).

Even if some of the magnetization that resides at shallow depths might be the result of materials delivered to the Moon during large impact events, the majority of magnetization is located at depths greater than about 10 km. The only explanation that remains for these regions is that the magnetic carriers formed at these depths at the same time as the primordial crust of the Moon. Though anorthositic rocks contain low abundances of metallic iron (e.g., Fuller & Cisowski, 1987), most of these regions are associated with low field strengths, especially when viewed in the magnetic field intensity plot of Figure 1 that uses a linear scale. Thermal evolution models predict that the highland crust would cool entirely below the Curie temperature of metallic iron (1038 K, Dunlop & Özdemir, 2015) within the first 100 Myr of lunar evolution (e.g., Arkani-Hamed & Boutin, 2017; Laneuville et al., 2017). Furthermore, most thermal evolution models predict that the core could have driven a dynamo powered by thermal convection during the first couple hundred million years (e.g., Evans et al., 2014; Konrad & Spohn, 1997; Laneuville et al., 2014; Scheinberg et al., 2015). Thus, the primordial deep crust was likely magnetized during the first 100 Myr of lunar evolution when a lunar dynamo was operating.

In summary, our results imply that the vast majority of the crust is heterogeneously magnetized over small scales, with the depth to the top of the magnetized region extending from the surface to about 25 km and with the bottom of this region extending probably to the base of the crust. The majority of the magnetic carriers found in the crust formed at the same time as the crust itself, and these materials became magnetized during the first 100 Myr of lunar evolution when the Moon had a dynamo-generated magnetic field. The projectiles that formed the Imbrium and South Pole-Aitken basins could have delivered some magnetic materials to the Moon as well and may account for some of the shallowest magnetization.

5.2. Origin of the Nearside Magnetic Low

The magnetic field intensity map of Figure 1 shows that the vast majority of the Moon's crust is at least partially magnetized. One major exception to this, which is best highlighted when plotting the field intensity logarithmically, is a large contiguous region on the nearside hemisphere centered at about (30°N, 20°W) where the field strengths are exceedingly weak (<0.1 nT at 30 km altitude). A considerably smaller region with similarly weak fields is found in the northern farside highlands near (70°N, 180°E). The weak crustal fields in these regions are not artifacts of the magnetic field map used in this study as maps of the surface field strength derived from the Lunar Prospector electron reflectometer also show weak fields in these same regions (Halekas et al., 2001; Mitchell et al., 2008). Our inversions show that these low field regions are associated with values of the square root of $N\langle M^2\rangle V^2$ that are 1 to 2 orders of magnitude lower than average. Three possible explanations can be considered for the origin of these prominent magnetic lows. The first is that they are related to demagnetization of the crust by impact events, the second is that they were never magnetized because of higher than average crustal temperatures, and the third is that these regions possess lower than average abundances of magnetic carriers. Though the abundance of magnetic carriers likely does

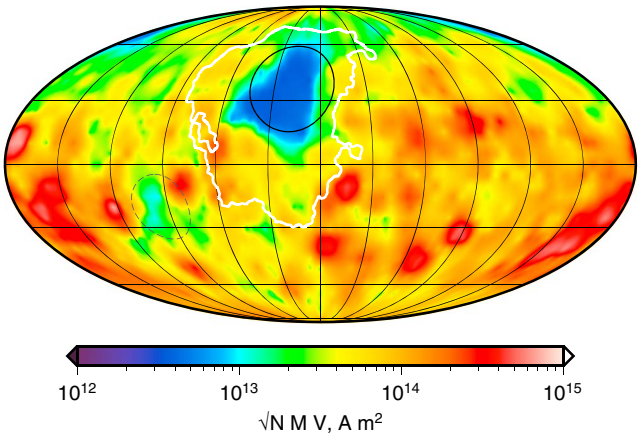

Figure 10. Confines of the Procellarum KREEP Terrane (white) and size of the Imbrium impact basin (black) superposed on the square root of $N\langle M^2\rangle V^2$. Inversion results are from Figure 7 and the contour plotted corresponds to the Procellarum KREEP Terrane, as defined here by abundances greater than 4.1 ppm Th from the map of Lawrence et al. (2003). For comparison with Figure 11, the confines of the Orientale impact basin (dashed) are also shown. Data are presented in a Mollweide projection centered on the prime meridian, and grid lines are spaced every 30° in latitude and longitude.

vary from place to place in the lunar crust, as we know of no way of testing this hypothesis, it will not be considered further.

The first explanation for the magnetic lows is that they are a result of crustal demagnetization related to large impact events. As seen in Figure 10, the near-side demagnetized zone does indeed correlate well with the Imbrium impact basin. The Imbrium basin is the largest basin on the nearside of the Moon and is one of the last three basins to have formed. It is well known that the shock waves generated during impact events are sufficient to partially demagnetize common magnetic minerals (e.g., Artemieva et al., 2005; Bezaeva et al., 2010; Gattacceca et al., 2010; Louzada et al., 2011), and several basins on both the Moon and Mars have been shown to have weaker than average magnetic field strengths in their interiors (e.g., Halekas et al., 2002, 2003; Langlais & Thébault, 2011; Lillis et al., 2010, 2013; Mohit & Arkani-Hamed, 2004). Thus, as originally proposed by Halekas et al. (2003), it should not be surprising that the Imbrium impact would partially demagnetize the surrounding crust, and that this impact is at least partially responsible for the magnetic low found in this region of the Moon. Regardless, it should be noted that the much smaller farside anomaly is not associated with any known impact basin.

There are couple of observations, however, that question whether the Imbrium impact is the sole cause of the nearside magnetic low. First, even though some impact basins have relatively low magnetic field strengths in their interiors, none have absolute strengths as low as those near the Imbrium basin, nor as large in spatial extent. As an example, as shown in Figure 11, the Orientale basin at (20.1°S, 265.2°E) is seen to have weak field strengths in its vicinity, but the size and magnitude of this anomaly are unlike those near the Imbrium basin. Furthermore, as shown in Figure 10, in contrast to the Imbrium basin, the Orientale basin is barely visible in our map of $N\langle M^2\rangle V^2$. Though it is true that Orientale is smaller than Imbrium (937 km in comparison to 1,321 km, Neumann et al., 2015), Orientale is not only one of the largest basins on

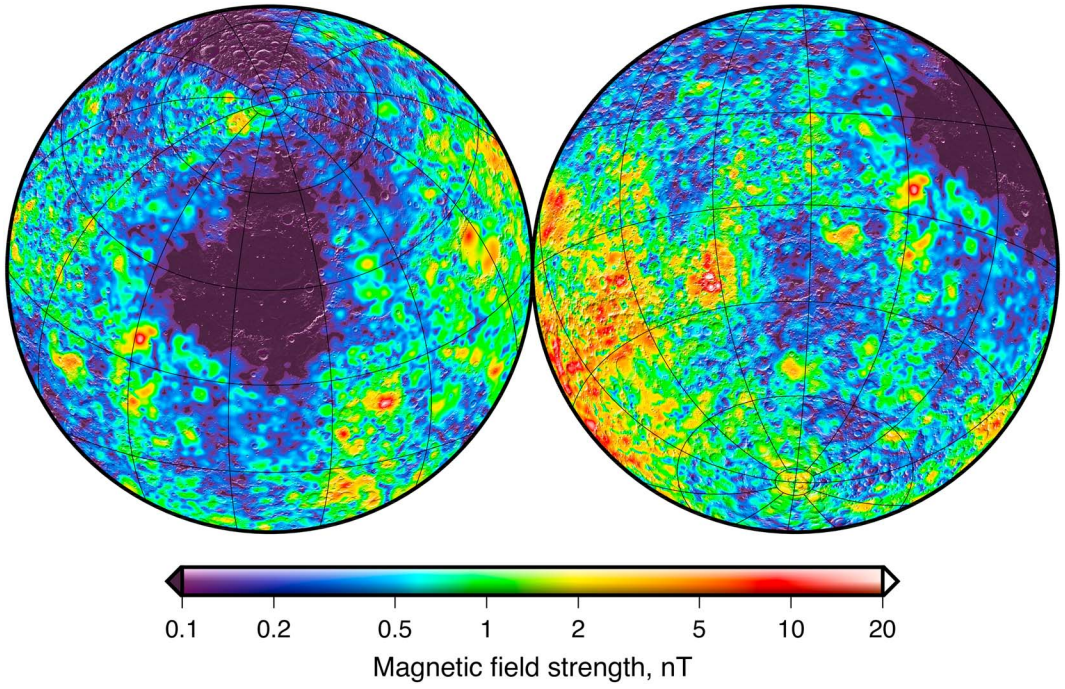

Figure 11. Total magnetic field strength of the Moon at 30 km altitude centered over the (left) Imbrium and (right) Orientale basins. The field strengths of Tsunakawa et al. (2015) are plotted using a logarithmic color scale, and the maps are presented in Lambert azimuthal equal-area projections overlain by a shaded relief map derived from the Lunar Orbiter Laser Altimeter (Smith et al., 2010). Grid lines are spaced every 30° in latitude and longitude.

the Moon but it is also younger than the Imbrium basin. The Crisium basin, which is the only basin intermediate in size between Imbrium and Orientale, does not have any clear demagnetization signature at all (in fact, its interior is strongly magnetized). The next largest basins of Serentitatis and Nectaris have annuli of weak fields surrounding a central high, but the magnitudes of the fields in the low-amplitude annuli are not comparable to those near the Imbrium basin. Finally, it is noted that even though the magnetic low encompasses most of the Imbrium basin, neither the maps of $N\langle M^2\rangle V^2$ nor the magnetic intensity are entirely symmetric about the basin center.

An alternative explanation for the prominent magnetic low on the nearside of the Moon is that it is instead related to high crustal temperatures that were above the blocking temperature of metallic iron at the time when the lunar dynamo was operating. As shown in Figure 10, the nearside magnetic low lies entirely within the confines of the Procellarum KREEP Terrane (PKT) (Jolliff et al., 2000), which is a geologic province that has high concentrations of the heat-producing elements potassium (K), uranium and thorium, the rare-Earth elements (REE), and phosphorous (P). The enrichment of these elements in the PKT appears to be related both to moderate enhancements of these elements in the mare basalts that erupted within this region and high concentrations in the underlying crust. In fact, exposures of highlands materials within this province that were not covered by mare basalts have considerably higher abundances of KREEP than the surrounding mare basalts themselves. This observation, when combined with the measured composition of materials that were excavated by the Imbrium impact event (Korotev, 2000), implies that the highest abundances of heat-producing elements reside within the crust, which is volumetrically more important than the thin surface veneer of mare basalts. Though the origin of this province is debated (see Shearer et al., 2006), it is related in some way to the final materials that crystallized from a global lunar magma ocean shortly after formation of the Earth-Moon system.

No other region of the Moon has enrichments in heat-producing elements, either at the surface or at depth, that are comparable to the Procellarum KREEP Terrane. The high heat production within this province certainly had a major influence on the thermal evolution of this region, and thermal evolution models predict the crust and underlying mantle of the PKT to have been considerably hotter than other regions of the Moon (Hess & Parmentier, 2001; Grimm, 2013; Laneuville et al., 2013; Wieczorek & Phillips, 2000). Indeed, these models predict the underlying mantle to have partially melted, giving rise to the mare basalts that erupted in the same region. It is thus conceivable that large portions of the crust within the PKT could have had temperatures above the Curie temperature of metallic iron at the same time when other regions of the highland crust had already cooled below this temperature.

If a strong dynamo field were present when the highland crust was cooling below the blocking temperature of iron, but not later when the crust of the PKT cooled below the same temperature, the crust of the PKT could escape becoming magnetized and would today be associated with a magnetic low. Thermal evolution models and paleomagnetic analyses of lunar rocks appear to be consistent with this scenario. Thermal evolution models predict that it could take more than 1 Gyr for the entire crust of the Procellarum KREEP Terrane to cool below the Curie temperature of metallic iron, as opposed to less than 100 Myr for the highland crust (Laneuville et al., 2017). Though a dynamo could have operated during this time (Laneuville et al., 2014; Scheinberg et al., 2015), paleomagnetic analyses suggest that the strength of the dynamo field weakened by more than an order of magnitude sometime after about 3.56 Ga (Tikoo et al., 2014; Weiss & Tikoo, 2014). Thus, large portions of the PKT could have cooled when the field strengths were considerably weaker than during the first 100 Myr of lunar evolution.

One consequence of this scenario is that the size of the Procellarum KREEP Terrane might be considerably smaller than once thought. The confines of the PKT are often delimited by those regions having thorium abundances greater than about 4 ppm thorium. However, the mare basalts in the PKT are thought to have moderate thorium enhancements, and portions of the underlying crust are likely to be considerably more enriched than the mare. Unfortunately, the confines of the region of the underlying crust with high thorium abundances is difficult to estimate given that this region was later resurfaced by mare basalts. We suggest here that the region of crust with extremely low magnetic field intensities might be a better indication of the size of the enhanced thorium abundances in the crust than are the surface abundances of the thorium. If this is true, the size of the PKT would be almost 3 times smaller than previous estimates.

The origin of the magnetic low in the northern farside highlands remains enigmatic. It does not appear to be associated with an impact basin, there is no associated enhancement of KREEP at the surface, and there is no

evidence for any volcanic activity in this region. One possible explanation for this magnetic low is that the crust in this region possesses lower than average abundances of metallic iron.

6. Conclusions

The problem of inverting for the depth and geometry of magnetic sources is notoriously difficult given that analyses of potential fields are inherently nonunique. To make progress on understanding the properties of crustal magnetization, it is often necessary to make assumptions about either the geometry of the magnetized sources or the direction of magnetization (e.g., Parker, 1991). In this analysis, the nonuniqueness problem was bypassed by making a few simple statistical assumptions about the sources. The magnetization was assumed to reside in an ensemble of magnetized sills or prisms with a specified size and range of depths. By assuming that the locations of the sources and magnetization directions were random, the model predicts a global power spectrum that depends upon the strength of magnetization, the size of the magnetized regions, and the depth range over which the magnetization is found. The model was shown to be insensitive to the assumed direction of magnetization, and for the longest wavelengths, the two models of sills and prisms were nearly identical.

Using this power spectrum model, a localized power spectrum analysis was used to invert for lateral variations in the model parameters. Our analysis showed that (1) the depth to the top of the magnetized region lies between the surface and about 25 km depth, (2) the depth to the bottom of the magnetized region was unconstrained, (3) the lateral size of the magnetic sources was less than about 30 km, and (4) the intensity of magnetization was extremely weak in a small region on the nearside hemisphere. It was argued that the magnetic sources in the deep crust were magnetized in the presence of a dynamo field when the crust cooled below the blocking temperature of metallic iron during the first 100 Myr of lunar evolution. Some magnetization that was located close to the surface may instead be partially a result of metallic iron delivered to the Moon by large impact events, such as the giant South Pole-Aitken impact. The region of low magnetization corresponds to the region where crustal fields are extremely weak, and although this anomaly could be a result of crustal demagnetization by the Imbrium impact, it was noted that its signature is atypical of other similarly sized impact basins. Instead, it was argued that this region of the crust was never magnetized as a result of prolonged high crustal temperatures that were present in the Procellarum KREEP Terrane. If the region of crust that is highly enriched in heat-producing elements corresponds to the size of the magnetic low, the size of the Procellarum KREEP Terrane could be about 3 times smaller than typically assumed.

Our analysis, however, leaves unresolved several problems related to lunar magnetism. For example, it was not possible to constrain the depth to the bottom of the magnetized region. Though it might be reasonable to assume that the maximum depth of magnetization would correspond to the base of the crust, in principle, it is possible that the upper mantle could host small quantities of metallic iron and that the upper mantle could also be partially magnetized (for a discussion concerning the possibility of magnetization in the upper mantle of Earth, see Ferré et al., 2014). The geometry of the magnetizing field is also not well understood, with both dipolar and highly quadrupolar fields being possible (e.g., Nayak et al., 2017; Oliveira & Wieczorek, 2017; Takahashi et al., 2014). If the field were predominantly dipolar, one might expect the strength of magnetization to vary by a factor of 2 from pole to equator, but this signal is not seen in our results. Nevertheless, one could argue that this factor of 2 would likely be overwhelmed by lateral variations in the abundance of magnetic carriers in the crust.

The time dependence of the strength of the dynamo field is also not well constrained. Though our results imply that a core dynamo must have operated earlier than the oldest paleomagnetic constraint of 4.25 Ga, neither the duration of the dynamo nor the evolution of its intensity is easily addressed from spacecraft measurements of crustal magnetism. If the magnetic low on the nearside is indeed a result of high crustal temperatures within the Procellarum KREEP Terrane, we can only say that the field strength decreased in intensity by more than an order of magnitude before this province cooled below the blocking temperature of metallic iron. Detailed thermal evolution models of the Procellarum KREEP Terrane could turn out to be invaluable for understanding not only the origin of the nearside magnetic low but also how the strength of the lunar dynamo evolved with time.

The results of this study could be improved upon in several ways. First, even though the most recent magnetic field models make use of Lunar Prospector and Kaguya vector magnetic field measurements, the spatial resolution of these fields is limited by the altitude of the measurements above the surface, which was about

30 km. In contrast, the Lunar Prospector electron reflectometer experiment directly sensed the magnetic field strength at the surface, and it is in principle possible to investigate the spectral properties of this total intensity field. This could potentially provide power spectrum estimates with higher spatial resolution that would better constrain the characteristic size of the magnetic sources and reduce the uncertainties on important model parameters. Second, our analysis assumed that the characteristic size of the magnetic sources was the same in each analysis region. Using our formalism, it would be straightforward to make use of a size-frequency distribution of magnetic sources. Though this might provide a more realistic description of crustal magnetism, and fit the available data better, the downside would be of having to introduce an additional parameter in our inversions. Finally, it is possible that remotely sensed spectroscopic data could be used to investigate the abundance of macroscopic metallic iron in the crust and how it varies with depth (e.g., Cahill et al., 2014). Results from such studies could not only be compared with geophysical inversions of the lunar magnetic field but also be used as an independent constraint on the abundance of magnetic carriers in the crust.

Appendix A: Gauss Coefficients of a Uniformly Magnetized Spherical Prism

The Gauss coefficients of a uniformly magnetized spherical prism are derived in this section. If the magnetization in the prism is constant in direction, as given by its three Cartesian coordinates,

$$\mathbf{M} = M_x\,\hat{\mathbf{x}} + M_y\,\hat{\mathbf{y}} + M_z\,\hat{\mathbf{z}}, \tag{A1}$$

then both the divergence of **M** and the volume integral in equation (2) are identically zero and the magnetic potential reduces to

$$U(\mathbf{r}') = \frac{\mu_0}{4\pi}\int_S \frac{\mathbf{M}(\mathbf{r})\cdot \mathrm{d}\mathbf{a}}{|\mathbf{r}'-\mathbf{r}|}. \tag{A2}$$

Calculation of the potential requires the evaluation of three surface integrals: two for the spherical interfaces that truncate the cone (surfaces I and II) and one for the surface of the cone between these interfaces (surface III). For this calculation, the axis of the cone will be assumed to coincide with the z axis, with the prism centered over the north pole.

For the upper interface (surface I), the area element is

$$\mathrm{d}\mathbf{a} = r_+^2\,\mathrm{d}\Omega\,\hat{\mathbf{r}}, \tag{A3}$$

where the Cartesian coordinates of the radial unit vector are

$$\hat{\mathbf{r}} = \sin\theta\cos\phi\,\hat{\mathbf{x}} + \sin\theta\sin\phi\,\hat{\mathbf{y}} + \cos\theta\,\hat{\mathbf{z}}. \tag{A4}$$

Using the definitions of the degree-1 Schmidt seminormalized spherical harmonic functions

$$Y_{10}(\theta,\phi) = \cos\theta \tag{A5}$$

$$Y_{11}(\theta,\phi) = \sin\theta\cos\phi \tag{A6}$$

$$Y_{1,-1}(\theta,\phi) = \sin\theta\sin\phi, \tag{A7}$$

the scalar product in the numerator in equation (A2) can be expressed as

$$\mathbf{M}(\mathbf{r})\cdot\mathrm{d}\mathbf{a} = r_+^2\,d\Omega\left(M_x\,Y_{11}(\theta,\phi) + M_y\,Y_{1,-1}(\theta,\phi) + M_z\,Y_{10}(\theta,\phi)\right). \tag{A8}$$

The denominator in equation (A2) can be simplified by making use of the identities

$$\frac{1}{|\mathbf{r}'-\mathbf{r}|} = \frac{1}{r'}\sum_{l=0}^{\infty}\left(\frac{r}{r'}\right)^l P_l(\cos\gamma) \quad \text{for } r' \geq r, \tag{A9}$$

$$P_l(\cos\gamma) = \sum_{m=-l}^{l} Y_{lm}(\theta,\phi)Y_{lm}(\theta',\phi'), \tag{A10}$$

where γ is the angle subtended between the vectors $\mathbf{r}$ and $\mathbf{r}'$. Combing the above equations yields the following expression for the integral over the upper surface:

$$U^{I}(\mathbf{r}') = \frac{\mu_0 r'}{4\pi} \sum_{l=0}^{\infty} \sum_{m=-l}^{l} \left(\frac{r_+}{r'}\right)^{l+2} Y_{lm}(\theta', \phi') \times \int_{I} Y_{lm}(\theta, \phi) \left[M_x Y_{11}(\theta, \phi) + M_y Y_{1,-1}(\theta, \phi) + M_z Y_{10}(\theta, \phi)\right] \mathrm{d}\Omega. \tag{A11}$$

For surface II, the differential surface area element is

$$\mathrm{d}\mathbf{a} = -r_-^2 \, \mathrm{d}\Omega \, \hat{\mathbf{r}}, \tag{A12}$$

and the derivation for the contribution to the potential differs only trivially from that for surface I. Given that the integration domain over the angular coordinates is the same for surfaces I and II, it is easily shown that the contribution to the potential from both surfaces is

$$U^{I+II}(\mathbf{r}') = \frac{\mu_0 r'}{4\pi} \sum_{l=0}^{\infty} \sum_{m=-l}^{l} \left[\left(\frac{r_+}{r'}\right)^{l+2} - \left(\frac{r_-}{r'}\right)^{l+2}\right] Y_{lm}(\theta', \phi') \times \int_{I,II} Y_{lm}(\theta, \phi) \left[M_x Y_{11}(\theta, \phi) + M_y Y_{1,-1}(\theta, \phi) + M_z Y_{10}(\theta, \phi)\right] \mathrm{d}\Omega. \tag{A13}$$

Finally, by performing the integral over ϕ from 0 to 2π, and taking into account the orthogonality properties of the sin and cos functions, we arrive at

$$U^{I+II}(\mathbf{r}') = \frac{\mu_0 r'}{2} \sum_{l=0}^{\infty} \sum_{m=-l}^{l} \left[\left(\frac{r_+}{r'}\right)^{l+2} - \left(\frac{r_-}{r'}\right)^{l+2}\right] Y_{lm}(\theta', \phi') \times \left[\frac{1}{2}\left(\delta_{m1} M_x + \delta_{m,-1} M_y\right) \int_{\cos\theta_0}^{1} \bar{P}_{l1}(x) \bar{P}_{11}(x) \, \mathrm{d}x + \delta_{m0} M_z \int_{\cos\theta_0}^{1} \bar{P}_{l0}(x) \bar{P}_{10}(x) \, \mathrm{d}x\right]. \tag{A14}$$

For surface III, the differential area element is

$$\mathrm{d}\mathbf{a} = r \sin\theta_0 \, \mathrm{d}r \, \mathrm{d}\phi \, \hat{\boldsymbol{\theta}}, \tag{A15}$$

where for our case with a constant colatitude

$$\hat{\boldsymbol{\theta}} = \cos\theta_0 \cos\phi \, \hat{\mathbf{x}} + \cos\theta_0 \sin\phi \, \hat{\mathbf{y}} - \sin\theta_0 \, \hat{\mathbf{z}}. \tag{A16}$$

Inserting the scalar product of $\mathbf{M} \cdot \mathrm{d}\mathbf{a}$ into equation (A2) yields

$$U^{III}(\mathbf{r}') = \frac{\mu_0 r'}{4\pi} \sum_{l=0}^{\infty} \sum_{m=-l}^{l} Y_{lm}(\theta', \phi') \int_{r_-}^{r_+} \frac{r^{l+1}}{r'^{l+2}} \mathrm{d}r \times \int_{0}^{2\pi} Y_{lm}(\theta_0, \phi) \, \sin\theta_0 \, \left(M_x \cos\theta_0 \cos\phi + M_y \cos\theta_0 \sin\phi - M_z \sin\theta_0\right) \mathrm{d}\phi \tag{A17}$$

Performing the integrals over r and ϕ yields

$$U^{III}(\mathbf{r}') = \frac{\mu_0 r'}{2} \sum_{l=0}^{\infty} \sum_{m=-l}^{l} Y_{lm}(\theta', \phi') \left[\left(\frac{r_+}{r'}\right)^{l+2} - \left(\frac{r_-}{r'}\right)^{l+2}\right] \times \frac{1}{(l+2)} \left[\frac{1}{2}\left(\delta_{m1} M_x + \delta_{m,-1} M_y\right) \bar{P}_{l1}(\cos\theta_0) \sin\theta_0 \cos\theta_0 - \delta_{m0} M_z \bar{P}_{l0}(\cos\theta_0) \sin^2\theta_0\right]. \tag{A18}$$

Combing equations (A14) and (A18), and making use of equation (3), the Gauss coefficients of the uniformly magnetized spherical prism are given by

$$g_{lm} = \frac{\mu_0}{2}\left[\left(\frac{r_+}{a}\right)^{l+2} - \left(\frac{r_-}{a}\right)^{l+2}\right] \times \left[\frac{1}{2}\left(\delta_{m1} M_x + \delta_{m,-1} M_y\right)\left(\int_{\cos\theta_0}^{1} \bar{P}_{l1}(x)\bar{P}_{11}(x)\,\mathrm{d}x + \frac{\bar{P}_{l1}(\cos\theta_0)\sin\theta_0\cos\theta_0}{(l+2)}\right) + \delta_{m0} M_z\left(\int_{\cos\theta_0}^{1} \bar{P}_{l0}(x)\bar{P}_{10}(x)\,\mathrm{d}x - \frac{\bar{P}_{l0}(\cos\theta_0)\sin^2\theta_0}{(l+2)}\right)\right]. \tag{A19}$$

Appendix B: Integrals of Associated Legendre Functions

The calculation of the theoretical power spectra in sections 2.2 and 2.3 can be simplified by noting that the Schmidt seminormalized Legendre functions and integrals of products of Legendre functions can be expressed in terms of ordinary Legendre polynomials and their first derivatives. We start with the formula for the integral of two (unnormalized) Legendre polynomials (e.g., Byerly, 1893, p. 172)

$$\int_x^1 P_l(x)\,P_m(x)\,\mathrm{d}x = \frac{\left(1-x^2\right)\left[P_m(x)\,P_l'(x) - P_l(x)\,P_m'(x)\right]}{l(l+1) - m(m+1)}, \quad l \neq m, \tag{B1}$$

where the first derivatives of the Legendre polynomials with respect to their argument are

$$P_l'(x) = \frac{-l\,x\,P_l(x) + l\,P_{l-1}(x)}{(1-x^2)}. \tag{B2}$$

With equations (B1) and (B2), the second integral in equation (23) can be expressed as

$$\int_{x_0}^{1} \bar{P}_{l0}(x)\bar{P}_{10}(x)\,\mathrm{d}x = \begin{cases} \mathrm{frac13}\left(1-x_0^3\right) & l = 1 \\ \frac{(1-x_0^2)}{(l+2)(l-1)}\left[x_0\,P_l'(x_0) - P_l(x_0)\right] & l \neq 1. \end{cases} \tag{B3}$$

Using the definition of the associated Legendre functions for $m = 1$

$$P_{l1}(x) = \sqrt{1-x^2}\,P_l'(x), \tag{B4}$$

the definition of the first derivative of the Legendre polynomials (equation (B2), the integral

$$\int_{x_0}^{1} P_l(x)\,\mathrm{d}x = \frac{(1-x_0^2)\,P_l'(x_0)}{l(l+1)}, \quad l \neq 0, \tag{B5}$$

and equation (B3), the first integral in equation (23) can be shown to be

$$\int_{x_0}^{1} \bar{P}_{l1}(x)\bar{P}_{11}(x)\,\mathrm{d}x = \begin{cases} \frac{2}{3} - x_0 + \frac{x_0^3}{3} & l = 1 \\ \sqrt{\frac{2}{l(l+1)}}\,\frac{(1-x_0^2)}{(l+2)(l-1)}\left[(l+2)P_{l-1}'(x_0) - l\,x_0\,P_l'(x_0) + l\,P_l(x_0)\right] & l \neq 1. \end{cases} \tag{B6}$$

Finally, using equation (B4), we have

$$\bar{P}_{l1}(\cos\theta) = \sqrt{\frac{2}{l(l+1)}}\,\sin\theta\,\mathrm{d}P_l(\cos\theta)/\mathrm{d}(\cos\theta). \tag{B7}$$

With equations (B3), (B6), and (B7), it is possible to calculate Z in equations (24), (25), (31), and (32) using only the standard Legendre polynomials and their first derivatives, which are easily calculated using well known recursion relationships.

Appendix C: Alternative Model Power Spectrum for Magnetized Sills

A model for the magnetic power spectrum was presented in section 2.3 that was the result of many thin spherical caps that were each magnetized in a random direction and that were randomly distributed between radii r_+ and r_-. For that model, the thickness of each sill was assumed to be constant, which implied that the sill volume depended on the radius at which it formed. In this section, results are presented where the sills are assumed to have a constant volume. Such thin caps could be thought of as magmatic sills. For this scenario, we multiply and divide the integrand of equation (27) by the area of each sill squared, $\left[2\pi(1-\cos\theta_0)\right]^2$, and replace the terms that correspond to the sill volume by the constant V_s. Integrating the equation, the total power spectrum of the collection of sills can be shown to be given by

$$\langle S_B(l)\rangle = N\langle M^2\rangle V_s^2 \frac{\mu_0^2}{V\,12\,\pi\,a^3\,(1-\cos\theta_0)^2} \frac{(l+1)(l+2)^2}{(2l+1)} \left[\left(\frac{r_+}{a}\right)^{2l+1} - \left(\frac{r_-}{a}\right)^{2l+1}\right] \times \left[\frac{1}{2}\left(\int_{\cos\theta_0}^{1} \bar{P}_{l1}(x)\bar{P}_{11}(x)\,\mathrm{d}x + \frac{\bar{P}_{l1}(\cos\theta_0)\sin\theta_0\cos\theta_0}{(l+2)}\right)^2 \right. \tag{C1}$$

$$\left. + \left(\int_{\cos\theta_0}^{1} \bar{P}_{l0}(x)\bar{P}_{10}(x)\,\mathrm{d}x - \frac{\bar{P}_{l0}(\cos\theta_0)\sin^2\theta_0}{(l+2)}\right)^2\right], \tag{C2}$$

where

$$V = \frac{4\pi}{3}\left(r_+^3 - r_-^3\right). \tag{C3}$$

Acknowledgments
This manuscript benefited from formal reviews by Peter James and an anonymous reviewer, as well as from comments by Coerte Voorhies, Doug Hemingway, and Benjamin Weiss. Data plotted in Figures 7–10, which represent the main results of the paper, can be downloaded from Zenodo (http://doi.org/10.5281/zenodo.1065898). All other figures can be easily reproduced from publicly available data and the *SHTOOLS* software package (Wieczorek et al., 2016). This work was supported by theFrench Agence Nationale de la Recherche (grant ANR-14-CE33-0012).

References

Acuña, M. H., Connerney, J. E. P., Ness, N. F., Lin, R. P., Mitchell, D., Carlson, C. W., … Cloutier, P. (1999). Global distribution of crustal magnetization discovered by the Mars Global Surveyor MAG/ER experiment. *Science*, *284*, 790–793. https://doi.org/10.1126/science.284.5415.790

Arkani-Hamed, J., & Boutin, D. (2014). Analysis of isolated magnetic anomalies and magnetic signatures of impact craters: Evidence for a core dynamo in the early history of the Moon. *Icarus*, *237*, 262–277. https://doi.org/10.1016/j.icarus.2014.04.046

Arkani-Hamed, J., & Boutin, D. (2017). South Pole Aitken Basin magnetic anomalies: Evidence for the true polar wander of Moon and a lunar dynamo reversal. *Journal of Geophysical Research: Planets*, *122*, 1195–1216. https://doi.org/10.1002/2016JE005234

Artemieva, N., Hood, L., & Ivanov, B. A. (2005). Impact demagnetization of the Martian crust: Primaries versus secondaries. *Geophysical Research Letters*, *32*, L22204. https://doi.org/10.1029/2005GL024385

Besserer, J., Nimmo, F., Wieczorek, M. A., Weber, R. C., Kiefer, W. S., McGovern, P. J., … Zuber, M. T. (2014). GRAIL gravity constraints on the vertical and lateral density structure of the lunar crust. *Geophysical Research Letters*, *41*, 5771–5777. https://doi.org/10.1002/2014GL060240

Bezaeva, N. S., Gattacceca, J., Rochette, P., Sadykov, R. A., & Trukhin, V. V. I. (2010). Demagnetization of terrestrial and extraterrestrial rocks under hydrostatic pressure up to 1.2 GPA. *Physics of the Earth and Planetary Interiors*, *179*, 7–20. https://doi.org/10.1016/j.pepi.2010.01.004

Blakely, R. J. (1995). *Potential theory in gravity and magnetic applications*. New York: Cambridge University Press.

Blanco, M. A., Flórez, M., & Bermejo, M. (1997). Evaluation of the rotation matrices in the basis of real spherical harmonics. *Journal of Molecular Structure*, *419*, 19–27.

Blewett, D. T., Hawke, B. R., Richmond, N. C., & Hughes, C. G. (2007). A magnetic anomaly associated with an albedo feature near Airy crater in the lunar nearside highlands. *Geophysical Research Letters*, *34*, L24206. https://doi.org/10.1029/2007GL031670

Bouligand, C., Glen, J. M. G., & Blakely, R. J. (2009). Mapping Curie temperature depth in the western United States with a fractal model for crustal magnetization. *Journal of Geophysical Research*, *114*, B11104. https://doi.org/10.1029/2009JB006494

Byerly, W. E. (1893). *An elementary treatise on Fourier's series and spherical, cylindrical, and ellipsoidal harmonics*. Boston, MA: Ginn and Company.

Cahill, J. T. S., Hagerty, J. J., Lawrence, D. J., Klima, R. L., & Blewett, D. T. (2014). Surveying the South Pole-Aitken basin magnetic anomaly for remnant impactor metallic iron. *Icarus*, *243*, 27–30. https://doi.org/10.1016/j.icarus.2014.08.035

Driscoll, J. R., & Healy, D. M. (1994). Computing Fourier transforms and convolutions on the 2-sphere. *Advances in Applied Mathematics*, *15*, 202–250. https://doi.org/10.1006/aama.1994.1008

Dunlop, D. J., & Özdemir, O. (2015). Magnetizations in rocks and minerals. *Treatise on Geophysics*, *5*, 255–308. https://doi.org/10.1016/B978-0-444-53802-4.00102-0

Dwyer, C., Stevenson, D., & Nimmo, F. (2011). A long-lived lunar dynamo driven by continuous mechanical stirring. *Nature*, *479*, 212–214. https://doi.org/10.1038/nature10564

Evans, A. J., Zuber, M. T., Weiss, B. P., & Tikoo, S. M. (2014). A wet, heterogeneous lunar interior: Lower mantle and core dynamo evolution. *Journal of Geophysical Research: Planets*, *119*, 1061–1077. https://doi.org/10.1002/2013JE004494

Ferré, E. C., Friedman, S. A., Martin-Hernandez, F., Feinberg, J. M., Till, J. L., Ionov, D. A., & Conder, J. A. (2014). Eight good reasons why the uppermost mantle could be magnetic. *Tectonophysics*, *624–625*, 3–14. https://doi.org/10.1016/j.tecto.2014.01.004

Fuller, M., & Cisowski, S. M. (1987). Lunar paleomagnetism. In J. A. Jacobs (Ed.), *Geomagnetism* (Vol. 2, pp. 307–455). London: Academic Press.

Garrick-Bethell, I., & Zuber, M. T. (2009). Elliptical structure of the lunar South Pole-Aitken basin. *Icarus*, *204*, 399–408. https://doi.org/10.1016/j.icarus.2009.05.032

Garrick-Bethell, I., Weiss, B. P., Shuster, D. L., & Buz, J. (2009). Early lunar magnetism. *Science*, *323*, 356–359.
Garrick-Bethell, I., Weiss, B. P., Schuster, D. L., Tikoo, S. M., & Tremblay, M. M. (2017). Further evidence for early lunar magnetism from troctolite 76535. *Journal of Geophysical Research: Planets*, *122*, 76–93. https://doi.org/10.1002/2016JE005154
Gattacceca, J., Boustie, M., Lima, E., Weiss, B., de Resseguier, T., & Cuq-Lelandais, J. (2010). Unraveling the simultaneous shock magnetization and demagnetization of rocks. *Physics of the Earth and Planetary Interiors*, *182*, 42–49. https://doi.org/10.1016/j.pepi.2010.06.009
Grimm, R. E. (2013). Geophysical constraints on the lunar Procellarum KREEP Terrane. *Journal of Geophysical Research: Planets*, *118*, 768–777. https://doi.org/10.1029/2012JE004114
Halekas, J., Mitchell, D., Lin, R., Frey, S., Hood, L., na, M. A., & Binder, A. (2001). Mapping of crustal magnetic anomalies on the lunar near side by the Lunar Prospector electron reflectometer. *Journal of Geophysical Research*, *106*, 27,841–27,852.
Halekas, J., Lin, R., & Mitchell, D. (2003). Magnetic fields of lunar multi-ring impact basins. *Meteoritics and Planetary Science*, *38*, 565–578.
Halekas, J. S., Mitchell, D. L., Lin, R. P., Hood, L. L., Acuña, M. H., & Binder, A. B. (2002). Demagnetization signatures of lunar impact craters. *Geophysical Research Letters*, *29*(13), 1645. https://doi.org/10.1029/2001GL013924
Hemingway, D., & Garrick-Bethell, I. (2012). Magnetic field direction and lunar swirl morphology: Insights from Airy and Reiner Gamma. *Journal of Geophysical Research*, *117*, E10012. https://doi.org/10.1029/2012JE004165
Hess, P. C., & Parmentier, E. M. (2001). Thermal evolution of a thicker KREEP layer. *Journal of Geophysical Research*, *106*, 28,023–28,032.
Hood, L. (2011). Central magnetic anomalies of Nectarian-aged lunar impact basins: Probable evidence for an early core dynamo. *Icarus*, *211*, 1109–1128.
Hood, L., Zakharian, A., Halekas, J., Mitchell, D., Lin, R., Acuña M. H., & Binder, A. (2001). Initial mapping and interpretation of lunar crustal magnetic anomalies using Lunar Prospector magnetometer data. *Journal of Geophysical Research*, *106*, 27,825–27,839.
Hood, L. L., Richmond, N. C., & Spudis, P. D. (2013). Origin of strong lunar magnetic anomalies: Further mapping and examinations of LROC imagery in regions antipodal to young large impact basins. *Journal of Geophysical Research: Planets*, *118*, 1265–1284. https://doi.org/10.1002/jgre.20078
Jackson, A. (1990). Accounting for crustal magnetization in models of the core magnetic field. *Geophysical Journal International*, *103*, 657–673.
Jackson, A. (1994). Statistical treatment of crustal magnetization. *Geophysical Journal International*, *119*, 991–998.
Jolliff, B. J., Gillis, J. J., Haskin, L. A., Korotev, R. L., & Wieczorek, M. A. (2000). Major lunar crustal terranes: Surface expressions and crust-mantle origins. *Journal of Geophysical Research*, *105*, 4197–4216.
Konrad, W., & Spohn, T. (1997). Thermal history of the Moon: Implications or an early core dynamo and post accretional magmatism. *Advances in Space Research*, *19*, 1511–1521.
Korotev, R. L. (2000). The great lunar hot spot and the composition and origin of the Appolo mafic ("LKFM") impact-melt breccias. *Journal of Geophysical Research*, *105*, 4317–4345.
Laneuville, M., Wieczorek, M. A., Breuer, D., & Tosi, N. (2013). Asymmetric thermal evolution of the Moon. *Journal of Geophysical Research: Planets*, *118*, 1435–1452. https://doi.org/10.1002/jgre.20103
Laneuville, M., Wieczorek, M. A., Breuer, D., Albert, J., Morard, G., & Rückriemen, T. (2014). A long-lived lunar dynamo powered by core crystallization. *Earth and Planetary Science Letters*, *401*, 251–260. https://doi.org/10.1016/j.epsl.2014.05.057
Laneuville, M., Taylor, J., & Wieczorek, M. (2017). *Radioactive heat sources distribution and magnetic fields, new views of the Moon 2, May 4–5*. Abstract 6019, Münster, Germany: LPI Contribution No. 1988.
Langlais, B., & Thébault, E. (2011). Predicted and observed magnetic signatures of Martian (de)magnetized impact craters. *Icarus*, *212*, 568–578. https://doi.org/10.1016/j.icarus.2011.01.015
Lawrence, D. J., Elphic, R. C., Feldman, W. C., Prettyman, T. H., Gasnault, O., & Maurice, S. (2003). Small-area thorium features on the lunar surface. *Journal of Geophysical Research*, *108*, 5102. https://doi.org/10.1029/2003JE002050
Le Bars, M., Wieczorek, M. A., Karatekin, Ö., Cébron, D., & Laneuville, M. (2011). An impact-driven dynamo for the early Moon. *Nature*, *479*, 215–218. https://doi.org/10.1038/nature10565
Lewis, K., & Simons, F. J. (2012). Local spectral variability and the origin of the Martian crustal magnetic field. *Geophysical Research Letters*, *39*, L18201. https://doi.org/10.1029/2012GL052708
Lillis, R. J., Purucker, M. E., Halekas, J. S., Louzada, K. L., Stewart-Mukhopadhyay, S. T., Manga, M., & Frey, H. V. (2010). Study of impact demagnetization at mars using Monte Carlo modeling and multiple altitude data. *Journal of Geophysical Research*, *115*, E07007. https://doi.org/10.1029/2009JE003556
Lillis, R. J., Robbins, S., Manga, M., Halekas, J. S., & Frey, H. V. (2013). Time history of the Martian dynamo from crater magnetic field analysis. *Journal of Geophysical Research: Planets*, *118*, 1488–1511. https://doi.org/10.1002/jgre.20105
Louzada, K. L., Stewart, S. T., Weiss, B. P., Gattacceca, J., Lillis, R. J., & Halekas, J. S. (2011). Impact demagnetization of the Martian crust: Current knowledge and future directions. *Earth and Planetary Science Letters*, *305*, 257–269. https://doi.org/10.1016/j.epsl.2011.03.013
Lowes, F. J. (1966). Mean-square values on sphere of spherical harmonic fields. *Journal of Geophysical Research*, *71*(8), 2179.
Mitchell, D. L., Halekas, J. S., Lin, R. P., Frey, S., Hood, L. L., Acuña, M. H., & Binder, A. (2008). Global mapping of lunar crustal magnetic fields by Lunar Prospector. *Icarus*, *194*, 401–409. https://doi.org/10.1016/j.icarus.2007.10.027
Mohit, P. S., & Arkani-Hamed, J. (2004). Impact demagnetization of the Martian crust. *Icarus*, *168*, 305–317. https://doi.org/10.1016/j.icarus.2003.12.005
Nayak, M., Hemingway, D., & Garrick-Bethell, I. (2017). Magnetization in the South Pole-Aitken basin: Implications for the lunar dynamo and true polar wander. *Icarus*, *286*, 153–192. https://doi.org/10.1016/j.icarus.2016.09.038
Neumann, G. A., Zuber, M. T., Wieczorek, M. A., Head, J. W., Baker, D. M. H., Solomon, S. C., … Kiefer, W. S. (2015). Lunar impact basins revealed by Gravity Recovery and Interior Laboratory measurements. *Science Advances*, *1*(9), e1500852. https://doi.org/10.1126/sciadv.1500852
Nicholas, J. B., Purucker, M. E., & Sabaka, T. J. (2007). Age spot or youthful marking: Origin of Reiner Gamma. *Geophysical Research Letters*, *34*, L02205. https://doi.org/10.1029/2006GL027794
Oliveira, J. S., & Wieczorek, M. A. (2017). Testing the axial dipole hypothesis for the moon by modeling the direction of crustal magnetization. *Journal of Geophysical Research: Planets*, *122*, 383–399. https://doi.org/10.1002/2016JE005199
Oliveira, J. S., Wieczorek, M. A., & Kletetschka, G. (2017). Iron abundances in lunar impact basin melt sheets from orbital magnetic field data. *Journal of Geophysical Research: Planets*, *122*, 2429–2444. https://doi.org/10.1002/2017JE005397
Parker, R. L. (1991). A theory of ideal bodies for seamount magnetism. *Journal of Geophysical Research*, *96*, 16,101–16,112.
Plattner, A., & Simons, F. J. (2017). Internal and external potential-field estimation from regional vector data at varying satellite altitude. *Geophysical Journal International*, *211*, 207–238. https://doi.org/10.1093/gji/ggx244
Purucker, M. E., & Nicholas, J. B. (2010). Global spherical harmonic models of the internal magnetic field of the Moon based on sequential and coestimation approaches. *Journal of Geophysical Research*, *115*, E12007. https://doi.org/10.1029/2010JE003650

Purucker, M. E., III, J. W. H., & Wilson, L. (2012). Magnetic signature of the lunar South Pole-Aitken basin: Character, origin, and age. *Journal of Geophysical Research*, *117*, E05001. https://doi.org/10.1029/2011JE003922

Richmond, N. C., Hood, L. L., Halekas, J. S., Mitchell, D. L., Lin, R. P., na, M. A., & Binder, A. B. (2003). Correlation of a strong lunar magnetic anomaly with a high-albedo region of the Descartes mountains. *Geophysical Research Letters*, *30*, 1395. https://doi.org/10.1029/2003GL016938

Richmond, N. C., Hood, L. L., Mitchell, D. L., Lin, R. P., na, M. H. A., & Binder, A. B. (2005). Correlations between magnetic anomalies and surface geology antipodal to lunar impact basins. *Journal of Geophysical Research*, *110*, E05011. https://doi.org/10.1029/2005JE002405

Scheinberg, A., Soderlund, K. M., & Schubert, G. (2015). Magnetic field generation in the lunar core: The role of inner core growth. *Icarus*, *254*, 62–71. https://doi.org/10.1016/j.icarus.2015.03.013

Shearer, C. K., Hess, P. C., Wieczorek, M. A., Pritchard, M. E., Parmentier, M. E., Borg, L. E., … Wiechert, U. (2006). Thermal and magmatic evolution of the Moon. In *New views of the Moon, Reviews in Mineralogy and Geochemistry* (Vol. 60, pp. 365–518). Washington, DC: Mineralogical Society of America.

Smith, D. E., Zuber, M. T., Neumann, G. A., Lemoine, F. G., Mazarico, E., Torrence, M. H., … Bartels, A. E. (2010). Initial observations from the Lunar Orbiter Laser Altimeter (LOLA). *Geophysical Research Letters*, *37*, L18204. https://doi.org/10.1029/2010GL043751

Suavet, C., Weiss, B. P., Cassata, W. S., Shuster, D. L., Gattacceca, J., Chan, L., … Fuller, M. D. (2013). Persistence and origin of the lunar core dynamo. *Proceedings of the National Academy of Sciences of the United States of America*, *110*, 8453–8458. https://doi.org/10.1073/pnas.1300341110

Takahashi, F., Tsunakawa, H., Shimizu, H., Shibuya, H., & Matsushima, M. (2014). Reorientation of the early lunar pole. *Nature Geoscience*, *7*, 409–412. https://doi.org/10.1038/NGEO2150

Thébault, E., & Vervelidou, F. (2015). A statistical spatial power spectrum of the Earth's lithospheric magnetic field. *Geophysical Journal International*, *201*, 605–620. https://doi.org/10.1093/gji/ggu463

Thébault, E., Schott, J. J., & Mandea, M. (2006). Revised spherical cap harmonic analysis (R-SCHA): Validation and properties. *Journal of Geophysical Research*, *111*, B01102. https://doi.org/10.1029/2005JB003836

Tikoo, S. M., Weiss, B. P., Cassata, W. S., Shuster, D. L., Gattacceca, J., Lima, E. A., … Fuller, M. D. (2014). Decline of the lunar dynamo. *Earth and Planetary Science Letters*, *404*, 89–97. https://doi.org/10.1016/j.epsl.2014.07.010

Tikoo, S. M., Weiss, B. P., Shuster, D. L., Suavet, C., Wang, H., & Grove, T. L. (2017). A two-billion-year history for the lunar dynamo. *Science of Advanced*, *3*, E1700207. https://doi.org/10.1126/sciadv.1700207

Tsunakawa, H., Takahashi, F., Shimizu, H., Shibuya, H., & Matsushima, M. (2015). Surface vector mapping of magnetic anomalies over the Moon using Kaguya and Lunar Prospector observations. *Journal of Geophysical Research: Planets*, *120*, 1160–1185. https://doi.org/10.1002/2014JE004785

Varshalovich, D. A., Moskalev, A. N., & Khersonskii, V. K. (1988). *Quantum theory of angular momentum*. Singapore: World Scientific.

Vervelidou, F., & Thébault, E. (2015). Global maps of the magnetic thickness and magnetization of the Earth's lithosphere. *Earth Planets Space*, *67*, 173. https://doi.org/10.1186/s40623-015-0329-5

Voorhies, C. V. (1998). Elementary theoretical forms for the spatial power spectrum of Earth's crustal field (Technical Paper 1998-20860838). Greenbelt, MD: NASA.

Voorhies, C. V. (2008). Thickness of the magnetic crust of Mars. *Journal of Geophysical Research*, *113*, E04004. https://doi.org/10.1029/2007JE002928

Voorhies, C. V., Sabaka, T. J., & Purucker, M. (2002). On magnetic spectra of Earth and Mars. *Journal of Geophysical Research*, *107*(E6), 5034. https://doi.org/10.1029/2001JE001534

Weiss, B. J., & Tikoo, S. M. (2014). The lunar dynamo. *Science*, *346*, 1246753. https://doi.org/10.1126/science.1246753

Wieczorek, M. A., & Phillips, R. J. (2000). The "Procellarum KREEP Terrane": Implications for mare volcanism and lunar evolution. *Journal of Geophysical Research*, *105*(E8), 20,417–20,430.

Wieczorek, M. A., & Simons, F. J. (2005). Localized spectral analysis on the sphere. *Geophysical Journal International*, *162*, 655–675. https://doi.org/10.1111/j.1365-246X.2005.02687.x

Wieczorek, M. A., & Simons, F. J. (2007). Minimum-variance multitaper spectral estimation on the sphere. *Journal of Fourier Analysis and Applications*, *13*, 665–692. https://doi.org/10.1007/ s00041-006-6904-1

Wieczorek, M. A., Weiss, B. P., & Stewart, S. T. (2012). An impactor origin for lunar magnetic anomalies. *Science*, *335*, 1212–1215. https://doi.org/10.1126/science.1214773

Wieczorek, M. A., Neumann, G. A., Nimmo, F., Kiefer, W. S., Taylor, G. J., Melosh, H. J., … Zuber, M. T. (2013). The crust of the Moon as seen by GRAIL. *Science*, *339*(6120), 671–675. https://doi.org/10.1126/science.1231530

Wieczorek, M. A., Meschede, M., Oshchepkov, I., Sales de Andrade, E., & heroxbd (2016). SHTOOLS: Version 4.0. *Zenodo*, 206114. https://doi.org/10.5281/zenodo.206114